Trachyte-phonolite transition at Dunedin Volcano: Fingerprints of magma plumbing system maturity and mush evolution

Pontesilli A. [1,2*], Brenna, M. [2], Mollo, S. [1,3], Masotta, M. [4], Nazzari, M. [1], Le Roux, P. [5], Scarlato, P. [1]

[1] Istituto Nazionale di Geofisica e Vulcanologia, Via di Vigna Murata 605, 00143 Rome, Italy
[2] Department of Geology, University of Otago, PO Box 56, Dunedin 9054, New Zealand
[3] Dipartimento di Scienze della Terra, Sapienza-Università di Roma, P.le Aldo Moro 5, 00185 Roma, Italy
[4] Dipartimento di Scienze della Terra, Università di Pisa, Via S. Maria 53, 56126 Pisa, Italy
[5] Department of Geological Sciences, University of Cape Town, Rondebosch 7701, South Africa

Corresponding author:
Alessio Pontesilli
Istituto Nazionale di Geofisica e Vulcanologia,
Via di Vigna Murata 605,
00143 Rome, Italy
Email: alessio.pontesilli@ingv.it

Abstract

Phonolite-trachyte associations are a common feature of alkaline volcanoes in intraplate settings, and their coexistence challenges closed-system magmatic differentiation scenarios. Here we have investigated the mineralogical and petrochemical features of dikes, lavas, pyroclastic deposits, and comagmatic crystal-rich enclaves outcropping at Dunedin Volcano (Otago region, southern New Zealand). These alkaline magmatic products show both highly and mildly alkaline affinities, trending towards phonolitic and trachytic end-members, respectively. Intermediate rocks are phonotephrites + tephriphonolites (highly alkaline series) and mugearites + benmoreites (mildly alkaline series) with a phenocryst assemblage of clinopyroxene + plagioclase ± amphibole formed at low to mid-crustal levels (i.e., ~29–16 km). Phonolites are porphyritic rocks characterized by alkali feldspar ± amphibole ± clinopyroxene. Their whole-rock compositions are highly enriched in incompatible elements, with variable Ba + Sr contents. A weak negative to slightly positive Eu anomaly is also associated with $^{87}Sr/^{86}Sr$ ratios of 0.7028–0.7031, which are comparable to those of parental magmas. Geochemical models indicate that phonolites originate as interstitial melts that are generated via abundant alkali feldspar crystallization from a shallow crystalline mush (i.e., ~14–5 km). Strong melt differentiation and extraction is testified by crystal-rich enclaves, as remnants of the mush region. On the other hand, trachytes are phenocryst-poor products strongly depleted in Ba + Sr and with a marked negative Eu anomaly. Trachytes are characterized by $^{87}Sr/^{86}Sr$ ratios of 0.7040–0.7060, which are different from intermediate rocks and phonolites, and trend towards crustal isotopic compositions. Integrated mass balance, trace element, and energy-constrained modeling confirm that trachytes originate from mildly alkaline magmas interacting with the country rock during feldspar fractionation. We interpret the transition from trachyte to phonolite formation and eruption resulting from the maturation of the plumbing system through accumulation, cooling, and degassing of both highly and mildly alkaline magmas.

Highlights:

- Thermobarometric constraints on the architecture of the magmatic plumbing system
- Phonolites and trachytes differentiate from intermediate magmas in the shallow crust
- Trachytes originate by assimilation and fractional crystallization
- Phonolites represent interstitial liquids of upper crustal mush regions
- Trachyte to phonolite transition relates to maturity of the magmatic plumbing system

Keywords: Dunedin Volcano; alkaline magmas; crystal-rich enclaves; trachyte-phonolite transition; crystalline mush evolution; magma fractionation and crustal assimilation.

1. Introduction

The association between phonolites and trachytes is typical of different volcanic settings worldwide, such as Mount Sidley volcano (Marie Byrd Land, Antarctica; Panter et al., 1997, 2021), Tenerife (Canary Islands, Spain; Sliwinski et al., 2015), Ulleung Island (South Korea; Brenna et al., 2014), Marquesas Islands, (French Polynesia; Legendre et al., 2005), Campi Flegrei (Italy; Forni et al., 2016), Darfur (NE Africa; Lucassen et al., 2013), Harrat Rahat (Saudi Arabia; Brenna et al., 2019). At alkaline intraplate volcanoes, phonolites and trachytes represent the most common evolved end-members of highly and mildly alkaline differentiation paths, respectively (Panter et al., 1997; White et al., 2012; Wright, 1971). Owing to the occurrence of a thermal barrier in the "Petrogeny's Residua System" (Wolff, 2017), phonolites cannot coexist with trachytes by simple closed-system fractional crystallization, and their petrogenesis is explained by a variety of mechanisms including assimilation of intrusive and/or country rock material, mush development/remobilization, and melt extraction (Bachmann et al., 2007; Brenna et al., 2019; Forni et al., 2016, 2018; Panter et al., 1997; Wolff et al., 2020). Although the origin of phonolitic magmas is usually attributed to high degrees of differentiation in the shallow crust, there are also field and petrographic evidences suggesting a deeper origin (e.g., Brenna et al., 2014; Grant et al., 2013).

At Dunedin Volcano (South Island, New Zealand), phonolites are interpreted as the result of feldspar fractionation at shallow crustal levels during late-stage evolution of highly alkaline magmas (Price, 1973; Price and Chappell, 1975; Price et al., 2003). In contrast, trachytes are supposed to originate by differentiation of mildly alkaline magmas with the contribution of crustal material and/or melting of crustal cumulates (Price and Compston, 1973).

In order to elucidate the differentiation processes and pre-eruptive storage conditions of phonolitic and trachytic magmas at Dunedin Volcano, we have investigated the petrographic

and compositional features of 29 volcanic rocks, including lavas, dykes, pyroclastic products, and crystal-rich enclaves. We defined the polybaric-polythermal differentiation of erupted magmas by integrating 1) mineral-melt equilibrium and thermobarometric constraints, 2) whole-rock trace element and Sr-Nd-Pb isotope modeling, and 3) energy-constrained thermal data. According to these new data, we propose that the compositional transition from trachytic to phonolitic melts is mostly governed by differentiation processes at shallow depth, where fractional crystallization and assimilation of crustal material occur before melt extraction and migration from a crystalline mush region.

2. Geological and petrological background

Dunedin Volcano represents one of the most voluminous examples of intraplate magmatism in the South Island of New Zealand, with volumes of erupted and intruded materials of ~150 and ~600 km^3, respectively (Coombs et al., 1986, 2008; Reilly, 1972). The main volcanic edifice formed over a prolonged period of activity between 16 and 11 Ma (Coombs et al., 2008; Hoernle et al. 2006; McDougall and Coombs, 1973; Scott et al., 2020). The activity at the periphery of the main edifice was more prolonged, ranging from 25 to 9 Ma. These eruptions developed monogenetic volcanic centers scattered over ~8000 km^2 in the Otago region (i.e., the "outlying flows" of the Dunedin Volcanic Group; Coombs et al., 1986; Scott et al., 2020). The eruptive epochs were categorized by Benson (1968) into three main phases of volcanism, plus an "Initial Eruptive Phase" that was dominated by mafic and intermediate products. During this initial phase, trachytic tephras and lava flows were also erupted (i.e., the "Koputai Trachyte", as defined by Allen, 1974). The activity was followed by more voluminous "First", "Second", and "Third" main eruptive phases, during which a wide range of rocks was emplaced (Benson, 1968). In particular, the last main stage was

characterized by the emplacement of lava domes with prevalent phonolitic composition (Price, 1973; Price and Coombs, 1975).

The Dunedin Volcano comprises a broad range of volcanic products, including basaltic lava flows and dykes, whereas pyroclastic flows and lava domes are typically characterized by more evolved compositions (Price and Coombs, 1975; Price et al., 2003). Larger and explosive eruptions were episodically fed by trachytic and phonolitic magmas, although alkaline basalts and trachybasalts dominated the eruptive record (Allen, 1974; Price, 1973; Price et al., 2003). In a study focusing on basalt whole-rock geochemistry, isotopic compositions and mineral cargoes, Pontesilli et al. (2021) modeled the degree of lithospheric and asthenospheric contribution in the genesis of high-alkali, mid-alkali and low-alkali basalts at Dunedin Volcano. In particular, high-alkali basalts were interpreted as the parental composition for highly alkaline intermediate magmas (phonotephrites), whereas mid-alkali basalts were hypothesized as the parental compositions of mildly alkaline intermediate magmas (mugearites). The distinct isotopic compositions of low-alkali basalts were related to asthenospheric melts. These results are in agreement with previous studies on Dunedin Volcano, indicating that trachytes and phonolites represent the most evolved products of mildly and highly alkaline magmas, respectively (Coombs and Wilkinson, 1969; Price, 1973; Price and Chappell, 1975).

Crystal-rich enclaves are commonly hosted in highly alkaline magmas, with textural and compositional features pointing to a cumulitic origin (Price et al., 2003). However, some syenites are interpreted as equivalents of felsic magmas solidified at shallow crustal levels (Price et al., 2003). Geophysical data also document the presence of voluminous intrusions within the Haast Schist basement, which extends from the upper crust to the lower crust (i.e., ~20–25 km; Godfrey et al., 2001).

3. Sampling and analytical methods

Since the investigation of primitive basalts has been the subject of recent work on the Dunedin Volcano (Pontesilli et al., 2021), in this study we have focused on intermediate and evolved products with both highly and mildly alkaline compositions. Sampling localities are reported in the schematic geological map displayed in Fig. 1, where phonotephrite + tephriphonolite (highly alkaline) and mugearite + benmoreite (mildly alkaline) are designated as P + T and M + B, respectively. A complete list of coordinates for sample locations is reported in Supplementary Material S1.

Major oxides in minerals (Supplementary Material S2) were measured with an electron probe micro-analyzer (EPMA), JEOL JXA 8200 equipped with five wavelength dispersive spectrometers (WDS) and installed at the HP-HT Laboratory of Experimental Volcanology and Geophysics of the Istituto Nazionale di Geofisica e Vulcanologia (INGV) in Rome (Italy). Carbon-coated thin sections were analyzed under an accelerating voltage and beam current of 15 kV and 10 nA, respectively. The beam size was 5 μm with a counting time of 20 and 10 seconds on peaks and background, respectively. Corrections for inter-elemental effects were made using a ZAF (Z, atomic number; A, absorption; F, fluorescence) procedure. The following standards were adopted for the various chemical elements: jadeite (Si and Na), corundum (Al), augite (Ca), forsterite (Mg), andradite (Fe), rutile (Ti), orthoclase (K), apatite (P), spessartine (Mn) and JEOL Cr metal. Sodium and potassium were analyzed first to minimize alkali migration effects. The analytical precision was assessed through well-characterized synthetic oxide and mineral standards. Data quality was ensured by measuring the same test materials as unknowns according to the procedure reported in Iezzi et al. (2014). Based on counting statistics, analytical uncertainties relative to their reported concentrations indicate that precision was better than 5% for all cations analyzed.

Whole-rock major and trace elements (Supplementary Material S3) were measured at the Australian Laboratory Services (ALS) Minerals in Brisbane. Loss on ignition was calculated as the difference between sample weights measured after heating to 105 °C and to 1000 °C. The ignited material was charged in a PtAu crucible, and then fused in a lithium tetraborate ($Li_2B_4O_7$) mixture. Major element concentrations were measured by X-Ray Fluorescence (XRF) using a Bruker S4 Pioneer system. For trace element analyses, fused disks made of dried sample powders and lithium tetraborate were dissolved in a mixture of HNO_3, HCl, and HF. Inductively coupled plasma - mass spectrometry (ICP-MS) analyses were carried out with a Perkin–Elmer Elan 9000 system. The quality of the data was verified against in-house standards and their duplicates were processed as unknowns. Data reproduction has been assessed through independent tests, indicating that the method yielded satisfactory results, with accuracy and precision better than 6% for all elements in concentrations above 1 wt.% and generally better than 10% for minor and trace elements.

Whole-rock isotopic analyses (Supplementary Material S3) were carried out with a NuPlasma HR multicollector ICP-MS installed at the Department of Geological Sciences, University of Cape Town, Rondebosch, South Africa. Sr, Nd, and Pb compositions were measured on a total of 11 whole-rock samples using the analytical procedure reported in Harris et al. (2015). Rock powder samples were dissolved in a HF/HNO_3 and converted to nitrates in a concentrated HNO_3 solution. Sr, Nd, and Pb fractions were isolated employing sequential column chemistry. Sr isotopic ratios were normalized to a value of 0.710255 for the NIST SRM987 reference material. Instrumental mass fractionation was evaluated through the exponential law and a $^{86}Sr/^{88}Sr$ ratio of 0.1194. Nd isotopic ratios were normalized to a value of 0.512115 for the Jndi-1 reference material. Instrumental mass fractionation was evaluated through the exponential law and against a $^{146}Nd/^{144}Nd$ ratio of 0.7219. Pb isotopic ratios were normalized to values of 36.7219 ($^{208}Pb/^{204}Pb$), 15.4963 ($^{207}Pb/^{204}Pb$), and 16.9405 ($^{206}Pb/^{204}Pb$)

for the NIST SRM981 reference material. Instrumental mass fractionation was evaluated through the exponential law and against a $^{205}Tl/^{203}Tl$ ratio of 2.3889. The analytical precision is given as 2σ errors in the last significant digits. The accuracy is below 0.1% for all isotopic ratios, with the exception of $^{208}Pb/^{204}Pb$ and $^{206}Pb/^{204}Pb$ ratios showing accuracy better than 0.2% and 0.5%, respectively. The accuracy was tested by using BHVO-2 as quality monitor. Sr and Nd isotopic ratios were corrected for an average age of 13 Ma, resulting from the radiometric dating of phonolites outcropping at the Dunedin Volcano (Coombs et al., 2008). Accordingly, $^{87}Sr/^{86}Sr$ and $^{143}Nd/^{144}Nd$ ratios reported in the text refer to the initial ratios.

4. Results

4.1 Petrography

4.1.1 Highly alkaline rocks

Phonotephrite lavas (PT1 and PT2), tephriphonolite dykes (TP1 and TP2), and a pyroclastic deposit (TP3; individual pumice samples) are porphyritic rocks (16–28 vol.%) with abundant mm-sized amphibole + clinopyroxene + titanomagnetite ± plagioclase phenocrysts (phase assemblages are given in order of abundance; Table 1, Supplementary Material S4). The µm-sized groundmass contains plagioclase + clinopyroxene + titanomagnetite ± amphibole ± alkali feldspar ± apatite. Amphibole has a red to dark brown to brown pleochroic scheme, while clinopyroxene is typically pinkish to grey under plane-polarized light (Fig. 2a). The pyroclastic sample TP3 comes from the Port Chalmers Breccia, one of the most voluminous pyroclastic units at Dunedin Volcano (Price et al., 2003).

Phonolite samples from domes (P1, P2, P3, P6, and P7) and dykes (P4, P5, P8 and P9) are both moderately porphyritic (P1, P2, P5, P6 and P9) and phenocryst-poor (P3, P4, P7, and P8). The phenocryst content is 7–43 vol.% and comprises alkali feldspar ± clinopyroxene ± amphibole ± nepheline ± titanomagnetite (Table 1, Supplementary Material S4). The

149 groundmass consists of alkali feldspar + clinopyroxene + titanomagnetite ± apatite.
150 Clinopyroxene is the main mafic phase in phonolites, as either single green crystals or coronas
151 of microcrystalline green clinopyroxenes and titanomagnetites overgrowing on pink resorbed
152 cores (Fig. 2b). Amphibole is strongly resorbed and replaced by a fine intergrowth of
153 titanomagnetite + clinopyroxene + feldspar (Fig. 2c).

154 Crystal-rich enclaves are represented by cm-sized fragments of holocrystalline syenites
155 and groundmass-bearing alkali feldspar-rich cumulates. FE3 and FE4 syenites are hosted in the
156 pyroclastic deposit (TP3) and phonolite lava (P1), respectively. These syenites are composed
157 of alkali feldspar + amphibole + titanomagnetite ± nepheline (Table 1, Supplementary Material
158 S4 and Fig. 2d). Alkali feldspar-rich cumulates FE1 and FE2 are highly porphyritic (phenocryst
159 content of 62–67 vol.%), with assemblage of alkali feldspar + amphibole + clinopyroxene +
160 titanomagnetite ± nepheline. The groundmass consists of μm-sized crystals of alkali feldspar +
161 clinopyroxene + titanomagnetite, resembling the matrix phases from tephriphonolite host rocks
162 (TP1 and TP2; Fig. 2e). Amphibole from syenites and feldspar-rich cumulates has green to
163 brown colors. Clinopyroxene from feldspar-rich cumulates is dark green, being
164 petrographically similar to phonolite host rocks.

165

166 *4.1.2 Mildly alkaline rocks*

167 Mugearite (M1, M2, M3 and M4) and benmoreite (B1, B2, B3, and B4) lavas show
168 similar phenocryst abundances (11–31 vol.%) and phase assemblages of plagioclase +
169 clinopyroxene + titanomagnetite ± amphibole ± alkali feldspar. The amphibole content is lower
170 than that found in highly alkaline rocks (Supplementary Material S4). The μm-sized
171 groundmass consists of plagioclase + clinopyroxene + titanomagnetite ± alkali feldspar ±
172 apatite. As for the case of highly alkaline products, amphibole exhibits red to brown
173 pleochroism, while clinopyroxene is pink to grey in color.

Trachytes (dyke T1, lava T2 and flow T3) are phenocryst-poor (phenocryst content of 6–10 vol.%) and contain phenocrysts of alkali feldspar ± plagioclase ± amphibole (Table 1). The groundmass consists of alkali feldspar + titanomagnetite ± clinopyroxene (Fig. 2f), also showing flow alignments that are characteristic of trachytic texture. Amphibole in T1 exhibits resorption textures and are characterized by a strong light to dark brown pleochroic scheme that is different from that observed in other rock types.

4.2 Mineral Chemistry

4.2.1 Clinopyroxene

Clinopyroxene compositions and components have been calculated according to the scheme of Putirka et al. (1996) and are reported in Supplementary Material S2. The value of Mg# has been also determined by the formula Mg / (Fe^{tot} + Mg) × 100, where major elements are expressed as cation fractions.

BSE photomicrographs show that clinopyroxene is present as both cognate phenocrysts (Fig. 3a) and antecrysts (i.e., resorbed cores; Fig. 3b). Cognate phenocrysts show variable core to rim compositions depicting a coherent evolutionary trend in terms of Mg# against Al + Ti (Fig. 4a). The chemistry of clinopyroxene can be divided in two main groups (Fig. 4a): 1) high-Mg# (53–81), high-Al + Ti (0.06–0.69 apfu) diopside-rich crystals from both highly and mildly alkaline products (Fig. 3a), and 2) low-Mg# (16–63), low-Al + Ti (0.03–0.27 apfu) hedenbergite-rich crystals from phonolites and crystal-rich enclaves. Notably, resorbed cores from these latter samples (Fig. 3b) show more primitive compositions (66–75 Mg# and 0.36–0.49 apfu Al + Ti), reproducing the chemistry of clinopyroxenes from less differentiated products (Fig. 4a).

4.2.2 Amphibole

Amphibole compositions and components have been recalculated by the method of Li et al. (2020), together with the value of Mg# [Mg / (Fe^{2+} + Mg) × 100] and Fe^{3+}/Fe^{2+} ratio in the lattice site.

As for the case of clinopyroxene, the plot of Mg# against Ti shows two distinct compositional groups (Fig. 4b): 1) high-Mg# (46–79), high-Ti (0.27–0.82 apfu) Kaersutite / Ti-rich Pargasite crystals from both highly and mildly alkaline products (Fig. 3c), and 2) low-Mg# (6–57), low-Ti (0.10–0.61 apfu) Hastingsite crystals from phonolites, trachytes, and crystal-rich enclaves (Fig. 3d, e). Amphibole phenocrysts from trachytes are the most differentiated (i.e., 6–13 Mg#; Fig. 4b). Overall, the value of Mg# monotonically decreases with decreasing Ti, suggesting a continuous differentiation path from primitive towards more differentiated magmas (Fig. 4b).

4.2.3 Feldspars

Plagioclase is ubiquitous in the studied products, with the exception of phonolites and crystal-rich enclaves. On the basis of anorthite (An), albite (Ab), and orthoclase (Or) end-members, the chemistry of plagioclase changes from An_{78} (labradorite) to An_{15} with (oligoclase) proceeding differentiation (Fig. 4c). The FeO^{tot} content ranges from 0.05 to 0.64 wt.%, and have no clear relation with An.

Alkali feldspar is present only in phonolites ($Ab_{38-84}Or_{10-62}$), crystal-rich enclaves ($Ab_{55-84}Or_{11-44}$), and trachytes ($Ab_{28-69}Or_{26-72}$) (Fig. 3f, Fig. 4c). The amount of FeO^{tot} is comprised within 0.02 and 0.59 wt.%, and slightly decrease with increasing Ab.

4.2.4 Titanomagnetite

Titanomagnetite phenocrysts from highly alkaline rocks exhibit FeO^{tot}, TiO_2, and ulvospinel (Usp) of 59–78 wt.%, 8–27 wt.%, and $Usp_{0.44–0.83}$, respectively. Titanomagnetite

crystals from phonolites have lower titanium contents ($Usp_{0.25–0.52}$) compared to the less evolved rock types.

Titanomagnetite phenocrysts from mildly alkaline rocks (i.e., 61–76 wt.% FeO^{tot}, 8–24 wt.% TiO_2, and $Usp_{0.21–0.81}$) are compositionally similar to those from crystal-rich enclaves (i.e., 62–75 wt.% FeO^{tot}, 11–25 wt.% TiO_2, and $Usp_{0.26–0.82}$).

4.3 Whole-rock geochemistry

4.3.1 Major elements

According to the total alkali vs. silica (TAS) diagram (Le Maitre et al., 2002) (Fig. 5a), volcanic rocks are classified as: 1) highly alkaline intermediate (i.e., phonotephrites and tephriphonolites; P + T) and evolved (i.e., phonolites) rocks, and 2) mildly alkaline intermediate (i.e., mugearites and benmoreites; M + B) and evolved (i.e., trachytes) rocks. The compositions of crystal-rich enclaves (i.e., syenites and feldspar-rich cumulates) are prevalently phonolites in the TAS diagram (Fig. 5a). This data set has been also integrated with whole-rock data from Allen (1974), Hoernle et al. (2006), Price et al. (2003), Scott et al. (2020) and Pontesilli et al. (2021) (Supplementary Material S3).

Binary oxide diagrams show that both volcanic rocks and crystal-rich enclaves align along a coherent evolutionary trend, where SiO_2 increases and MgO (Fig. 5b), CaO (Fig. 5c) and FeO^{tot} (Fig. 5d) progressively decrease. Al_2O_3 also increases with increasing SiO_2, showing a plateau effect at $SiO_2 \geq 51$ wt.% (Fig. 5e). Trachytes and phonolites are the most differentiated products, whereas the whole-rock composition of crystal-rich enclaves resembles that of phonolites. In terms of Mg#, the magmatic differentiation proceeds 1) from M + B ($Mg\#_{27-40}$) to trachytes ($Mg\#_{13-16}$) for the mildly alkaline series, and 2) from P + T ($Mg\#_{27-38}$) to phonolites ($Mg\#_{4-32}$) for the highly alkaline series.

4.3.2 *Trace elements*

Chondrite-normalized patterns (McDonough and Sun, 1995) of rare earth elements (REE) are displayed in Fig. 6a-b. Light and heavy REE (i.e., LREE and HREE, respectively) in phonolites (312–700 La_N and 17–29 Yb_N; Fig. 6a) and trachytes (340–614 La_N and 25–42 Yb_N; Fig. 6b) are systematically higher than those of P + T (308–375 La_N and 14–18 Yb_N; Fig. 6a) and M + B (247–355 La_N and 15–20 Yb_N; Fig. 6b) rocks. Sub-parallel trends shift towards progressive REE enrichments from less differentiated to more evolved whole-rock compositions. Higher ratios of LREE relative to HREE are observed in highly alkaline rocks when compared to mildly alkaline rocks, with La_N/Yb_N ratios of 18–27 (P + T), 17–25 (phonolites), 14–23 (M + B), and 13–15 (trachytes). There is also a decrease of LREE/HREE with magma differentiation in both mildly alkaline and highly alkaline rock series.

Primordial mantle-normalized patterns (McDonough and Sun, 1995) of trace elements are displayed in Fig. 6c-d. Large-ion lithophile elements (LILE; i.e., Ba, Sr) and Eu are progressively depleted from P + T (94–144 Ba_N, 37–49 Sr_N, and 15–18 Eu_N; Fig. 6c) and M + B (98–127 Ba_N, 28–49 Sr_N, and 17–21 Eu_N; Fig. 6d) to phonolites (25–145 Ba_N, 5–68 Sr_N and 7–20 Eu_N; Fig. 6c) and trachytes (6–23 Ba_N, 1–2 Sr_N, 5–8 Eu_N; Fig. 6d), respectively. Ti_N and P_N are also depleted in the more evolved rocks, with values of 1–10 and 0.2–1.1 (phonolites), 1–4 and 0.2–0.3 (trachytes), 14–31 and 1.4–2.4 (P + T), and 15–26 and 1.2–3.1 (M + B), respectively. The Eu anomaly ($\frac{Eu}{Eu^*} = \frac{Eu_N}{\sqrt{Gd_N \times Sm_N}}$) is close to 1 for both P + T and M + B. Conversely, $\frac{Eu}{Eu^*}$ decreases to 0.55 and 0.24 in phonolites and trachytes, respectively. Crystal-rich enclaves show Eu anomaly within a broad interval, from 0.53 to 1.62. The concentration of Ba in highly alkaline products is also higher than that measured for mildly alkaline rocks. On the other hand, incompatible Rb and high field strength elements (HFSE; i.e., Nb and Zr) are progressively enriched from P + T (69–239 Rb_N, 123–227 Nb_N, 38–51 Zr_N) and M + B

(116–168 Rb_N, 120–184 Nb_N, 31–48 Zr_N) to phonolites (187–460 Rb_N, 163–359 Nb_N, 62–115 Zr_N) and trachytes (265–458 Rb_N, 225–363 Nb_N, 77–117 Zr_N), respectively.

4.3.3 Sr, Nd, Pb isotopes

Initial Sr, Nd, and Pb isotopic compositions of highly alkaline rocks cluster in relatively narrow ranges of $^{87}Sr/^{86}Sr$ (0.7028–0.7029), $^{143}Nd/^{144}Nd$ (0.51288–0.51291), $^{208}Pb/^{204}Pb$ (39.56–39.80), $^{207}Pb/^{204}Pb$ (15.65–15.66), and $^{206}Pb/^{204}Pb$ (19.99–20.29). Intermediate mildly alkaline rocks show similar $^{207}Pb/^{204}Pb$ (15.65–15.66) with slightly higher $^{87}Sr/^{86}Sr$ (0.7029–0.7032) and lower $^{143}Nd/^{144}Nd$ (0.51286–0.51291), $^{208}Pb/^{204}Pb$ (39.32–39.57), and $^{206}Pb/^{204}Pb$ (19.60–20.02). Crystal-rich enclaves are characterized by more variable isotopic compositions, with $^{87}Sr/^{86}Sr$ (0.7028–0.7033), $^{143}Nd/^{144}Nd$ (0.51286–0.51291), $^{208}Pb/^{204}Pb$ (39.18–39.55), $^{207}Pb/^{204}Pb$ (15.62–15.65), and $^{206}Pb/^{204}Pb$ (19.53–19.87). Overall these isotopic signatures lie on a trend that is defined by the literature data on Dunedin Volcano (Scott et al., 2020). According to Pontesilli et al. (2021), this trend relates the different contributions of lithospheric and asthenospheric melts to the whole-rock geochemistry (see isotopic data and plots reported in Supplementary Material S3). The only notable exception to this general trend is represented by trachytes that, with respect to intermediate mildly alkaline rocks, show higher $^{87}Sr/^{86}Sr$ (0.7049–0.7060) but comparable $^{143}Nd/^{144}Nd$ (0.51287–0.51289), $^{208}Pb/^{204}Pb$ (39.24–39.43), $^{207}Pb/^{204}Pb$ (15.65–15.66), and $^{206}Pb/^{204}Pb$ (19.52–19.85).

5. Discussions

5.1 Magma storage conditions

To retrieve the crystallization conditions of highly and mildly alkaline magmatic series, equilibrium and partitioning models for clinopyroxene (Blundy et al., 1995; Mollo et al., 2013; Mollo and Masotta, 2014; Putirka, 2008), amphibole (Putirka, 2016), plagioclase (Putirka,

298 2005), alkali feldspar (Mollo et al., 2015a), and titanomagnetite (Aryaeva et al., 2018), have
299 been applied to verify the attainment of near-equilibrium between selected crystal compositions
300 and bulk rock analyses. The equilibrium pairs have also been compared with a comprehensive
301 whole-rock data set available for the Dunedin Volcano (Scott et al. 2020), by means of a root-
302 mean square procedure. Given that crystal-rich enclaves and clinopyroxene resorbed cores are
303 unlikely to be in equilibrium with magmas (e.g., Ziberna et al., 2017), these populations were
304 not used to estimate magma storage conditions. The equilibrium models have been integrated
305 with thermobarometric (Glazner, 1984; Namur et al., 2012; Perinelli et al., 2016; Putirka, 2016;
306 Putirka et al., 1996), hygrometric (Masotta and Mollo, 2019; Mollo et al., 2015a; Putirka,
307 2008), and oxygen barometric (Ariskin and Nikolaev, 1996) equations, in order to minimize
308 any potential uncertainty in P-T-H_2O-fO_2 estimates and to track the crystallization conditions
309 of the bulk system. A detailed description of this approach is reported in Supplementary
310 Material S5.

311 Results from probability density functions indicate that intermediate to evolved
312 magmas were stored at polybaric-polythermal conditions under variable melt-H_2O
313 concentrations (Figs. 7, 8, and 9). Specifically, clinopyroxene, amphibole, and plagioclase
314 phenocrysts yield conditions of 596–666 ± 170 MPa (representing respectively the range of
315 average estimates and the mean standard deviation), 1022–1058 ± 39 °C and 1.7–2.4 ± 0.9
316 wt.% H_2O for intermediate highly alkaline magmas. On the other hand, intermediate mildly
317 alkaline magmas evolved at 675–684 ± 167 MPa, 1021–1061 ± 43 °C, and 1.9–2.1 ± 0.8 wt.%
318 H_2O (Figs. 7, 8, and 9). As illustrated in the schematic sketch drawn in Fig. 10, our estimates
319 depict overall low-to-mid crustal reservoirs at ~16–29 km depth, considering an average
320 continental crustal density of 2800 kg m^{-3} and a mantle-crust boundary at ~30 km (Godfrey et
321 al., 2001). Similar depth conditions are estimated by Pontesilli et al., (2021) for alkaline basalts
322 at Dunedin Volcano, suggesting the juxtaposition of primitive and intermediate reservoirs

within the crust (Fig. 10). Early differentiation of alkaline basalts proceeded by fractional crystallization of olivine + clinopyroxene + titanomagnetite, whereas amphibole segregated only from more differentiated magmas (Pontesilli et al., 2021; Price and Chappell, 1975). Coherently, amphibole saturation amphibole (1030–1038 ± 30 °C) occurs at a lower temperature than that of clinopyroxene (1058–1061 ± 54 °C), in good agreement with phase equilibrium experiments conducted by Nekvasil et al., (2004) on alkaline compositions (i.e., 430–930 MPa, 940–1250 °C, 0–5.1 wt.% H_2O, and ΔFMQ from -0.5 to -1.5).

Lower *P-T* conditions and higher melt-H_2O contents are determined for phonolites (~230–245 ± 87 MPa, 855–916 ± 51 °C, and 6.1 ± 1.1 wt.% H_2O) and trachytes (191 ± 13 MPa, 820–869 ± 28 °C, and 6.5–6.8 ± 0.7 wt.% H_2O) (Figs. 7, 8, and 9). These estimates corroborate the development of shallow crustal reservoirs at ~5–14 km (Fig. 10). Crystal-rich enclaves are also interpreted to derive from the same depth range as phonolites, based on the observation that phenocrysts from both crystal-rich enclaves and phonolites share virtually identical compositions (Fig. 4a, b, d). The occurrence of more hydrous magmas can be related to the higher degree of crystallization driving the differentiation of alkaline compositions (e.g., Masotta et al., 2013; Mollo et al., 2015b). Experimental results also support the increased solubility of H_2O in more evolved magmas, in good agreement with melt-H_2O contents estimated in this study. For trachytes, a water saturation threshold of ~7 wt.% at ~200 MPa has been estimated (Di Matteo et al., 2004), whereas water saturation ranges of ~6 and ~8 wt.% are measured in phonolitic melt at 150 and 300 MPa, respectively (Schmidt & Behrens, 1998).

The high melt-H_2O content of trachytes and phonolites (Fig. 9) and the attainment of water saturation at shallow depth is likely to stabilize amphibole (Fig. 2d-e; Supplementary Material S4). Conversely, amphibole reaction rims are likely the result of degassing phenomena during magma ascent and decompression (D'Mello et al., 2021).

As the amount of H_2O increases towards the saturation state of the melt, the Fe-Ti exchange in titanomagnetite may reflect more oxidizing crystallization conditions (Del Bello et al., 2014; Mollo et al., 2015c and references therein). Coherently, highly and mildly alkaline rocks record fO_2 conditions (-0.11 ± 0.64 and -0.46 ± 0.96 ΔFMQ, respectively) lower than those measured for phonolites (1.10 ± 1.25 ΔFMQ) and crystal-rich enclaves (1.53 ± 1.22 ΔFMQ; Fig. 9). For differentiated alkaline volcanic systems, fO_2 has been documented to increase by 1 to 2 log units via H_2O exsolution and, eventually, degassing (Del Bello et al., 2014; Palummo et al., 2020). This causes the redox state of the melt to change, thereby leading to the different incorporation of Fe^{3+} and Ti^{4+} cations during titanomagnetite crystallization.

5.2 Magma-mush dynamics: The origin of phonolites

The coexistence of highly and mildly alkaline trends at Dunedin Volcano are mainly attributed to different fractional crystallization assemblages and to distinct parental compositions (Coombs and Wilkinson, 1969; Price and Chappell, 1975; Pontesilli et al., 2021). Phonolites are also hypothesized to develop at the late stage of differentiation of highly alkaline magmas via abundant fractionation of alkali feldspar (Coombs et al., 2008; Price and Chappell, 1975; Price et al., 2003). In order to provide quantitative constraints on magma differentiation processes, we have modeled whole-rock major oxides by the least square mass balance criterion developed by Stormer and Nicholls (1978). According to the modal abundance, average mineral compositions have been subtracted to the whole-rock chemistry on an anhydrous basis (see Supplementary Material S6). An alkali feldspar-dominated phase assemblage (>70%) is required to fractionate phonolites from highly alkaline compositions (i.e., tephriphonolite TP1). Conspicuous crystal residues are difficult to reconcile with fractional crystallization in a closed-system, as the residual melt would remain locked within the crystalline network (Dufek and Bachmann, 2010).

Therefore, to further test the fractional crystallization hypothesis for the origin of phonolites, we have modeled the geochemical behavior of trace elements through the Rayleigh fractional crystallization equation:

$$C_l = C_0 \, F^{D-1} \quad (1)$$

where C_0 and C_l are the concentrations of trace elements of interest in the parental liquid and in the remaining melt, respectively. F stands for the melt fraction. The bulk partition coefficient (D) is calculated as:

$$D = \sum_i x_i \, K_i \quad (2)$$

where x_i is the weight fraction of mineral phase i and K_i is the partition coefficient of the element of interest. The most appropriate partition coefficients for differentiated alkaline magmas have been selected from literature (e.g., Larsen et al., 1979; Lemarchand et al., 1987; Villemant, 1988). The optimal set of partition coefficients for the given starting compositions was refined by comparing modeled and observed trace element patterns in natural rocks. The value of F has been modulated according to the mineral modal abundance in natural rocks and results from mass balance calculations. A complete list of input and output parameters is reported in Supplementary Material S6.

FC vectors for Ba vs. Zr (Fig. 11a) and Sr vs. Rb (Fig. 11b) fail to reproduce the differentiation of highly alkaline magmas. Indeed, trace element paths point to marked Sr + Ba depletions not observed in phonolites. This implausible deviation of modeled FC vectors reinforces the hypothesis that highly alkaline evolved magmas are generated by extraction of interstitial melts from crystal mush zones at shallow levels (e.g., Bachmann and Huber, 2016; Forni et al., 2016; Masotta et al., 2016; Brenna et al., 2019; Palummo et al., 2020). The upward extraction of differentiated melts from the mush can be driven by compaction and hindered settling (Bachmann and Bergantz; 2004), the failure of the growing crystal network at the roof of the solidification front (Marsh, 2002; Masotta et al., 2016), or disturbance by later magma

injections (Brenna et al. 2019). According to thermomechanical modeling of Huber et al. (2019), the optimal depth for the storage extracted melts is typically between 250 and 150 MPa (i.e., the depth range of crystal-rich enclaves displayed in Fig. 10), where melts pond at the apex of a series of interconnected magma transfer zones.

Abundant crystal-rich enclaves are typically found in association with highly alkaline rocks (e.g., phonolites) and their mineral and whole-rock compositions indicate a cogenetic origin (Figs. 4 and 5). Additionally, alkali feldspar accumulation in the shallow crust provides the principal means for syenite formation (e.g. Bachmann et al., 2007; Glazner et al., 2018; Masotta et al., 2016; Wolff et al., 2015). Phonolitic melts typically represent the interstitial liquids of extensive low-pressure crystallization of a feldspar-rich assemblage (Wolff et al., 2015). In agreement with this model, the groundmass mineral assemblage and texture of cumulates resemble those observed for phonolites (Figs. 2b, e, 10; Table 1), thereby pointing to the origin of feldspar cumulates as remnants of a crystalline mush. This hypothesis is supported by mass balance modeling reproducing major element compositions of phenocryst-poor phonolites (P2, P3), as residue after removal of 49% alkali feldspar + 9% amphibole + 2% titanomagnetite + 1% apatite from feldspar-rich cumulates (Supplementary Material S6).

To further explore the differentiation of highly alkaline magmas and trace element inventory of melts extracted from the crystalline mush, the in-situ crystallization (ISC) equation of Langmuir (1989) has been employed:

$$C_l = C_0 \, F^{[F(D-1))/(D(1-f)+f]} \quad (3)$$

C_0, C_l, F, and D are defined as for Eq. (1). The parameter f represents the fraction of residual melt returned from the crystal mush zone to the crystallizing magmatic reservoir. Its value ranges from 0 (i.e., no residual melts return to the magmatic reservoir) to 1 (i.e., all the interstitial melt returns to the free melt and Eq. (3) reduces to the simple form of Eq. (1)). The fraction of residual melt is set between 0.3 and 0.5, in agreement with the optimum crystallinity

422 window (i.e., 50–70%) for crystal–melt separation (Dufek and Bachmann, 2010). The ISC
423 vector may shift downward (or upward) with increasing (or decreasing) *f*, accounting for the
424 contribution of residual melts trapped and extracted from the crystalline mush. This modulates
425 also the enrichment and depletion of incompatible and compatible trace elements.

426 ISC trends have been derived for Ba vs. Zr (Fig. 11a), Sr vs. Rb (Fig. 11b), Yb vs. La
427 (Fig. 11c), and Eu/Eu* vs. Nb (Fig. 11d). These trends reproduce very well the trace element
428 contents and variability of phonolites via late-stage alkali feldspar crystallization, as the
429 proportion of interstitial melt migrating from the solidification front decreases from 80%
430 (ISC1) to 40% (ISC2). Scattered Ba and Sr enrichments in phonolites are modeled by a green
431 vector (see Fig. 11a-b) that indicates entrainment of alkali feldspar (i.e., max 30%) in the
432 phonolitic melt. Indeed, alkali feldspar phenocrysts can be scavenged from the crystal mush by
433 the extracted residual liquid (e.g., Molina et al., 2012; Wieser et al., 2019), justifying the highly
434 variable alkali feldspar modal contents (5-32 vol.%) in phonolites.

435 Segregation of differentiated melts by gravitational instability at the top of a
436 solidification front has been proposed as possible mechanism for the eruption of crystal-poor
437 magmas stored in shallow reservoirs (Marsh, 2002; Masotta et al., 2012). At the same time,
438 injections of more primitive magmas that breaks into the crystalline mush may trigger eruption
439 of differentiated, crystal-poor melts (e.g., Brenna et al., 2019; Costa et al., 2021; Forni et al.,
440 2016; Szymaniowsky et al., 2017). Such fresh magma injections are represented by the
441 resorbed cores in clinopyroxene phenocrysts from phonolites and crystal-rich enclaves (Fig.
442 2b, 3b). In this context, eruption of intermediate to evolved magmas is typically associated with
443 the occurrence of abundant comagmatic enclaves (e.g., Costa et al., 2020), also indicative of
444 the cannibalization of the crystalline mush (Cashman and Blundy, 2013).

445

446 ***5.3 Assimilation and fractional crystallization: The origin of trachytes***

Trachytes are characterized by marked depletions in CaO, Sr, and Ba, with also negative Eu/Eu* anomaly that differs markedly from phonolites (Figs. 5 and 6). Results from mass balance calculations confirm the origin of trachytes from mugearitic magma (i.e., sample M2) due to fractionation of a phase assemblage dominated by feldspar (i.e., 21% alkali feldspar + 19% plagioclase + 10% clinopyroxene + 7% amphibole + 3% titanomagnetite; Supplementary Material S6). However, Sr isotopes of trachytes (i.e., $^{87}Sr/^{86}Sr > 0.7040$) deviate significantly from the isotopic range of intermediate magmas at Dunedin Volcano (i.e., $^{87}Sr/^{86}Sr$ ratios from 0.7028 to 0.7033; Fig. 11e). This deviation has been qualitatively related to crustal assimilation processes (Price and Chappell, 1975; Price and Compston, 1973). Here, we tested this hypothesis by the assimilation and fractional crystallization (AFC) equation of DePaolo (1981):

$$C_l = C_0 \left[F^{-z} + \left(\frac{r}{r-1}\right)\frac{C_a}{z\,C_0}\,(1 - F^{-1})\right] \quad (4)$$

where C_0, C_l, D, and F are defined as in Eq. (1). C_a represents the concentration of the modeled element in the contaminant, whereas r is the mass ratio of assimilated to crystallized material. The parameter z is defined as:

$$z = (r + D - 1)/(r - 1) \quad (5)$$

For the composition of the assimilated material, we have used the trace element and isotopic compositions of basement rocks from the Otago region (i.e., Haast Schists; Scanlan et al., 2020), with r variable from 0.1 to 0.2. Low mass ratios of assimilated material to crystalline residue are to be expected in small-scale magma bodies crystallizing at shallow crustal levels (Kuritani et al., 2005). The values of F and mineral phase proportions come from mass balance calculations (Supplementary Materials S6). Ba against Zr (Fig. 11a) and Sr against Rb (Fig. 11b) diagrams show that the compositions of trachytes can be reproduced by AFC vectors involving a main modal assemblage of 20% alkali feldspar + 15% plagioclase + 10% clinopyroxene + 5% amphibole + 3% titanomagnetite. In a similar fashion, the fractionation of

472 a feldspar-dominated assemblage reproduces the increase of incompatible Yb and La (Fig.
473 11c), as well as the marked negative Eu/Eu* anomaly (Fig. 11d). Importantly, AFC vectors are
474 consistent with Sr and Nd isotopic changes of trachytes (Fig. 11e-f), also in comparison with
475 data reported by Price and Compston (1973) (see Supplementary Material S3).

476 To effectively characterize the energy balance of country rock assimilation, we used
477 the energy-constrained assimilation–fractional crystallization (EC-AFC) algorithm of Spera
478 and Bohrson (2001). The input parameters are the same as for AFC modeling, whereas thermal
479 boundary conditions are based on temperature estimates (Fig. 8). The energy-constrained
480 model indicates that the lowest $^{87}Sr/^{86}Sr$ ratio of 0.7039 for trachytes is related to 5%
481 assimilated material and 48% crystalline residue (Fig. 12a). In contrast, the highest $^{87}Sr/^{86}Sr$
482 ratio of 0.7060 is due to 15% assimilated material and 60% crystalline residue (Fig. 12a).

483 Country rock assimilation occurs when the heat provided by the intruding magma
484 exceeds the energy needed to heat and partially melt the country rock. If we consider that
485 magma at temperature T_m intrudes a country rock at T_a, and magma-country rock interaction
486 develops at equilibrium temperature T, then the minimum condition for assimilation may be
487 expressed as (modified after Reiners et al., 1995):

488 $$M_c \Delta H_f^c + M_m C_p^m \Delta T_a = M_a \Delta H_f^a + M_a C_p^a \Delta T_a \quad (6)$$

489 M_m, M_c, and M_a represents the mass of magma, fractionated crystals, and assimilant,
490 respectively. $C_p{}^a$ and $C_p{}^m$ are the specific isobaric heat capacities (J K^{-1} g^{-1}) for assimilant and
491 magma, respectively. $C_p{}^a$ has been estimated via thermodynamic simulations based on the
492 Rhyolite-MELTS algorithm (v.1.2.0; Gualda et al., 2012) conducted for both solid and melt
493 assimilant fractions (see Supplementary Material S7 for further details). $C_p{}^m$ has been estimated
494 with the T-dependent model of Stebbins et al. (1984). $\Delta H_f{}^a$ and $\Delta H_f{}^c$ are the specific enthalpy
495 of fusion (J g^{-1}) for assimilant and solid fractions, respectively. These thermodynamic
496 quantities have been determined using mineral enthalpies from published data sets (Ghiorso,

2004; Lesher & Spera, 2015; Robie et al., 1995), considering a basement lithology composed of quartz + alkali feldspar + muscovite (cf. Scanlan et al., 2020). The solid residue results from the crystallization of a mugearite (i.e., sample M2) recognized as the progenitor of trachytes (Fig. 11; Supplementary Materials S6). MELTS thermodynamic simulations have been performed at 600–250 MPa, 1050–800 °C, 2.5 wt.% $H_2O_{initial}$, FMQ, as derived by previous mineral-melt constraints (cf. Figs. 7, 8, and 9). This data set provided the relative proportions of M_c and M_m, as well as the maximum degree of country rock partial melting. Eq. (6) has been solved for a country rock at initial T_a = 350 °C (i.e., depth of ~10 km, assuming a geothermal gradient of 35 °C/km) and initial magma mass (M_m^0 = 1) at T_m = 1050 °C (see Supplementary Material S7 for further details). Results from calculations are plotted in Fig. 12b showing that the thermal range of trachytic magmas (i.e., $T \leq 925$ °C) is consistent with the assimilation of small amounts of crustal material (5–15% relative to the initial mass of magma). Within this thermal range, M_a is much lower than M_c, according to a M_a/M_c ratio between 0.10 and 0.25. This result corroborates the low mass ratios of assimilated country rock adopted in AFC modelling. Moreover, the heat released by the intruding magma significantly exceeds the heat required to assimilate the country rock (Fig. 12b), thus supporting the efficacy of AFC processes in influencing the trace element and isotopic signature of trachytic magmas. Assimilation of crustal material has been shown by Harris (1995) to control silica saturation in evolved rocks from the Damaraland complexes (NW Namibia). Mildly alkaline rocks from our study are characterized by constant normative compositions, being mostly nepheline-normative to slightly hypersthene-normative (Supplementary Material S3). Nonetheless, quartz-normative trachytes with high $^{87}Sr/^{86}Sr$ also occur at Dunedin Volcano (Price & Compston, 1973; Price & Chappell, 1975; Scott et al., 2020), indicating that crustal assimilation may have played a role in promoting silica saturation of some erupted trachytes.

5.4 Plumbing system maturity: trachyte-phonolite transition

Spatial and temporal compositional heterogeneities in magmas are likely to derive from the long lifespan of Dunedin Volcano (i.e., ~5 Ma; Scott et al., 2020), in concert with variable inputs of asthenospheric melts and melting degrees of lithospheric lithologies (Pontesilli et al., 2021). Given the long life-span of activity it is unlikely that a centralized plumbing system was active throughout the history of the volcano. Instead, localized development of magma reservoirs is likely to have fed intermediate to evolved dispersed centers, such as Karitane (McLeod & White, 2018). Specifically, stratigraphic and geochronologic constraints on the eruptive products indicate that phonolites occurred mostly at the latest stage of activity, being mainly erupted between 11.0 ± 0.2 and 12.8 ± 0.3 Ma (Benson, 1968; Coombs, 1965; Coombs et al., 2008; McDougall & Coombs, 1973; Price, 1973). In contrast, mildly alkaline products are stratigraphically related to the early stage of volcanic activity (Allen, 1974), with geochronological data indicating an age comprised between 13.1 ± 0.3 and 14.2 ± 0.3 Ma (Coombs et al., 2008; McDougall & Coombs, 1973).

Following this line of reasoning, we observe that the assimilation of country rock material involved only the differentiation of mildly alkaline magmas to trachytes, prior to differentiation of the phonolites (Fig. 11e-f). The late crystallization of phonolites occurred also at temperatures higher than trachytes (Fig. 8), suggesting that heat exchange with the country rock was less efficient during the differentiation of highly alkaline magmas. According to the stratigraphic and geochronologic constraints, it is likely that early mugearitic and benmoreitic injections opened the path towards upper crustal levels where they formed trachytic reservoirs later intruded by highly alkaline magmas to form crystalline mush layers. Re-working of crustal pathways may also explain the similar storage depths estimated for highly and mildly alkaline magma series (Fig.10). Results of melting experiments and thermodynamic modelling by Meade et al. (2014) revealed that, although crustal sections not

previously affected by magma intrusion are highly fusible, repeated heating events will make the crust more refractory over time. Crustal pre-conditioning by previous trachytic injections would be capable of shielding crustal lithologies and inhibiting magma-country rock interaction, as the magmatic intrusions tend to follow pre-established crustal pathways (Thiele et al., 2021).

Transitions between trachyte and phonolite magmas is a typical characteristic of intraplate volcanic systems worldwide (e.g. Thompson et al., 2001; White et al., 2012). Trachytes with high radiogenic Sr were also analyzed by Panter et al. (1997) at Marie Byrd Land (Australia). Assimilation and fractional crystallization produced trachytes from fast ascending parental magmas, whereas phonolites differentiated by abundant feldspar fractionation from more alkaline magmas ponding in the upper crust (Panter et al., 1997). At Ulleung volcano (South Korea), Park et al. (2020) suggested that syenitic intrusions were generated after inputs of alkaline melts in trachytic reservoirs, also anticipating phonolitic eruptions. Therefore, abundant volumes of phonolites (Coombs, 1965; Price, 1973) in the eruptive record point to the development of a complex plumbing system where trachyte to phonolite transition marks an important stage in the maturity of the shallow crystalline mush (Fig. 10). Younger phonolitic magmas developed at the mature stage of Dunedin Volcano via melt segregation and accumulation within a crystal-rich framework over a prolonged time (>100 ka; Bachmann & Huber; 2019; Szymanowski et al., 2017).

6. Conclusions

In this contribution the differentiation of intermediate to evolved magma compositions at Dunedin Volcano has been investigated by means of whole-rock major and trace element and isotope analyses. Mineral chemistry of phenocrysts in equilibrium with their host magmas have been used to reconstruct magma storage conditions. Highly alkaline (phonotephrite-

572 tephriphonolite) and mildly alkaline (mugearite-benmoreite) magmas crystallize
573 clinopyroxene, amphibole, and plagioclase at low-to-mid crustal depths (~16–29 km). Magma
574 ascent towards upper crustal levels (~5–14 km) is accompanied by abundant crystallization of
575 a feldspar-dominated phase assemblage at low temperatures. At these shallow crustal levels,
576 the formation of more differentiated phonolitic and trachytic magmas is related to a range of
577 processes, including crystal fractionation, assimilation of crustal lithologies, and interaction
578 between ascending magmas and crystal mush zones in the shallow portions of the plumbing
579 system. Trachytes are produced by intrusion of mildly alkaline magmas in the upper crust,
580 where extensive cooling and crystallization provide enough heat to induce partial melting and
581 small degree of country rock assimilation. Conversely, phonolites are produced by extraction
582 of interstitial melts from crystalline mush regions. Remnants of the mush framework are
583 testified by crystal-rich enclaves (i.e., syenites and feldspar cumulates) entrained within highly
584 alkaline melts. Geochronologic and stratigraphic evidences show that eruption of trachytic
585 magmas preceded the emplacement of phonolites. Therefore, the transition between trachyte
586 and phonolite eruptions may be the final expression of magma plumbing system maturity.
587
588 **Acknowledgements**
589 Thanks go to A. Cooper, M. Palin, J. Scott, A.D. Weaver, J.D.L. White and L. Ziberna
590 for the insightful discussions. We are grateful to Ben Ellis and Kurt Panter for insightful
591 reviews that greatly helped to improve the manuscript and Michael Roden for his editorial
592 work. B. Pooley is also acknowledged for helping with sample preparation. Part of this work
593 has been supported by a PhD scholarship from the University of Otago.
594
595 **References**

596 Ariskin, A.A., Nikolaev, G.S., 1996. An empirical model for the calculation of spinel-
597 melt equilibria in mafic igneous systems at atmospheric pressure: 1. Chromian spinels. Contrib
598 Mineral Petrol 123, 282–292. https://doi.org/10.1007/s004100050156
599 Aryaeva, N.S., Koptev-Dvornikov, E.V., Bychkov, D.A., 2018. A Liquidus
600 Thermobarometer for Modeling of the Magnetite–Melt Equilibrium. Moscow Univ. Geol. Bull.
601 73, 177–186. https://doi.org/10.3103/S0145875218020023
602 Bachmann, O., Bergantz, G.W., 2004. On the Origin of Crystal-poor Rhyolites:
603 Extracted from Batholithic Crystal Mushes. J Petrology 45, 1565–1582.
604 https://doi.org/10.1093/petrology/egh019
605 Bachmann, O., Miller, C.F., de Silva, S.L., 2007. The volcanic–plutonic connection as
606 a stage for understanding crustal magmatism. Journal of Volcanology and Geothermal
607 Research, Large Silicic Magma Systems 167, 1–23.
608 https://doi.org/10.1016/j.jvolgeores.2007.08.002
609 Bachmann, O., Huber, C., 2019. The Inner Workings of Crustal Distillation Columns;
610 the Physical Mechanisms and Rates Controlling Phase Separation in Silicic Magma Reservoirs.
611 J Petrology 60, 3–18. https://doi.org/10.1093/petrology/egy103
612 Benson, W. N. (1968). Dunedin District. 1: 50000. New Zealand Geological Survey
613 miscellaneous series map, 1, 1-18.
614 Blundy, J.D., Falloon, T.J., Wood, B.J., Dalton, J.A., 1995. Sodium partitioning
615 between clinopyroxene and silicate melts. Journal of Geophysical Research: Solid Earth 100,
616 15501–15515. https://doi.org/10.1029/95JB00954
617 Brenna, M., Price, R., Cronin, S.J., Smith, I.E.M., Sohn, Y.K., Kim, G.B., Maas, R.,
618 2014. Final Magma Storage Depth Modulation of Explosivity and Trachyte–Phonolite Genesis
619 at an Intraplate Volcano: a Case Study from Ulleung Island, South Korea. J Petrology 55, 709–
620 747. https://doi.org/10.1093/petrology/egu004

Brenna, M., Pontesilli, A., Mollo, S., Masotta, M., Cronin, S.J., Smith, I.E.M., Moufti, M.R.H., Scarlato, P., 2019. Intra-eruptive trachyte-phonolite transition: Natural evidence and experimental constraints on the role of crystal mushes. American Mineralogist 104, 1750–1764. https://doi.org/10.2138/am-2019-6963

Cashman, K., Blundy, J., 2013. Petrological cannibalism: the chemical and textural consequences of incremental magma body growth. Contrib Mineral Petrol 166, 703–729. https://doi.org/10.1007/s00410-013-0895-0

Coombs, D. S. (1965). Dunedin volcanic complex and Waipiata volcanic formation. *New Zealand Department of Scientific and Industrial Research, Information Series*, *51*, 54-67.

Coombs, D.S., Wilkinson, J.F.G., 1969. Lineages and Fractionation Trends in Undersaturated Volcanic Rocks from the East Otago Volcanic Province (New Zealand) and Related Rocks. J Petrology 10, 440–501. https://doi.org/10.1093/petrology/10.3.440

Coombs, D. S., Cas, R. A., Kawachi, Y., Landis, C. A., McDonough, W. F., & Reay, A. (1986). Cenozoic volcanism in north, east and central Otago. Royal Society of New Zealand Bulletin, 23, 278-312.

Coombs, D.S., Adams, C.J., Roser, B.P., Reay, A., 2008. Geochronology and geochemistry of the Dunedin Volcanic Group, eastern Otago, New Zealand. New Zealand Journal of Geology and Geophysics 51, 195–218. https://doi.org/10.1080/00288300809509860

Costa, S., Masotta, M., Gioncada, A., Pistolesi, M., Bosch, D., Scarlato, P., 2020. Magma evolution at La Fossa volcano (Vulcano Island, Italy) in the last 1000 years: evidence from eruptive products and temperature gradient experiments. Contrib Mineral Petrol 175, 31. https://doi.org/10.1007/s00410-020-1669-0

Costa, S., Masotta, M., Gioncada, A., Pistolesi, M., 2021. A Crystal Mush Perspective Explains Magma Variability at La Fossa Volcano (Vulcano, Italy). Minerals 11, 1094. https://doi.org/10.3390/min11101094

D'Mello, N.G., Zellmer, G.F., Negrini, M., Kereszturi, G., Procter, J., Stewart, R., Prior, D., Usuki, M., Iizuka, Y., 2021. Deciphering magma storage and ascent processes of Taranaki, New Zealand, from the complexity of amphibole breakdown textures. Lithos 398–399, 106264. https://doi.org/10.1016/j.lithos.2021.106264

DePaolo, D.J., 1981. Trace element and isotopic effects of combined wallrock assimilation and fractional crystallization. Earth and Planetary Science Letters 53, 189–202. https://doi.org/10.1016/0012-821X(81)90153-9

Di Matteo, V., Carroll, M.R., Behrens, H., Vetere, F., Brooker, R.A., 2004. Water solubility in trachytic melts. Chemical Geology, 7th Silicate Melt Workshop 213, 187–196. https://doi.org/10.1016/j.chemgeo.2004.08.042

Dufek, J., Bachmann, O., 2010. Quantum magmatism: Magmatic compositional gaps generated by melt-crystal dynamics. Geology 38, 687–690. https://doi.org/10.1130/G30831.1

Forni, F., Bachmann, O., Mollo, S., De Astis, G., Gelman, S.E., Ellis, B.S., 2016. The origin of a zoned ignimbrite: Insights into the Campanian Ignimbrite magma chamber (Campi Flegrei, Italy). Earth and Planetary Science Letters 449, 259–271. https://doi.org/10.1016/j.epsl.2016.06.003

Forni, F., Degruyter, W., Bachmann, O., Astis, G.D., Mollo, S., 2018. Long-term magmatic evolution reveals the beginning of a new caldera cycle at Campi Flegrei. Science Advances 4, eaat9401. https://doi.org/10.1126/sciadv.aat9401

Ghiorso, M.S., 2004. An equation of state for silicate melts. III. Analysis of stoichiometric liquids at elevated pressure: shock compression data, molecular dynamics simulations and mineral fusion curves. Am J Sci 304, 752–810. https://doi.org/10.2475/ajs.304.8-9.752

669 Glazner, A.F., 1984. Activities of olivine and plagioclase components in silicate melts
670 and their application to geothermometry. Contr. Mineral. and Petrol. 88, 260–268.
671 https://doi.org/10.1007/BF00380170
672 Godfrey, N.J., Davey, F., Stern, T.A., Okaya, D., 2001. Crustal structure and thermal
673 anomalies of the Dunedin Region, South Island, New Zealand. Journal of Geophysical
674 Research: Solid Earth 106, 30835–30848. https://doi.org/10.1029/2000JB000006
675 Grant, T.B., Milke, R., Pandey, S., Jahnke, H., 2013. The Heldburg Phonolite, Central
676 Germany: Reactions between phonolite and xenocrysts from the upper mantle and lower crust.
677 Lithos 182–183, 86–101. https://doi.org/10.1016/j.lithos.2013.09.012
678 Gualda, G.A.R., Ghiorso, M.S., Lemons, R.V., Carley, T.L., 2012. Rhyolite-MELTS:
679 a Modified Calibration of MELTS Optimized for Silica-rich, Fluid-bearing Magmatic Systems.
680 J Petrology 53, 875–890. https://doi.org/10.1093/petrology/egr080
681 Harris, C., 1995. Oxygen isotope geochemistry of the Mesozoic anorogenic complexes
682 of Damaraland, northwest Namibia: evidence for crustal contamination and its effect on silica
683 saturation. Contrib Mineral Petrol 122, 308–321. https://doi.org/10.1007/s004100050130
684 Harris, C., le Roux, P., Cochrane, R., Martin, L., Duncan, A.R., Marsh, J.S., le Roex,
685 A.P., Class, C., 2015. The oxygen isotope composition of Karoo and Etendeka picrites: High
686 δ18O mantle or crustal contamination? Contrib Mineral Petrol 170, 8.
687 https://doi.org/10.1007/s00410-015-1164-1
688 Hoernle, K., White, J.D.L., van den Bogaard, P., Hauff, F., Coombs, D.S., Werner, R.,
689 Timm, C., Garbe-Schönberg, D., Reay, A., Cooper, A.F., 2006. Cenozoic intraplate volcanism
690 on New Zealand: Upwelling induced by lithospheric removal. Earth and Planetary Science
691 Letters 248, 350–367. https://doi.org/10.1016/j.epsl.2006.06.001

692 Huber, C., Townsend, M., Degruyter, W., Bachmann, O., 2019. Optimal depth of
693 subvolcanic magma chamber growth controlled by volatiles and crust rheology. Nat. Geosci.
694 12, 762–768. https://doi.org/10.1038/s41561-019-0415-6
695 Iezzi, G., Mollo, S., Shahini, E., Cavallo, A., Scarlato, P., 2014. The cooling kinetics
696 of plagioclase feldspar as revealed by electron-microprobe mapping. American Mineralogist
697 99, 898–907. https://doi.org/10.2138/am.2014.4626
698 Kuritani, T., Kitagawa, H., Nakamura, E., 2005. Assimilation and Fractional
699 Crystallization Controlled by Transport Process of Crustal Melt: Implications from an Alkali
700 Basalt–Dacite Suite from Rishiri Volcano, Japan. J Petrology 46, 1421–1442.
701 https://doi.org/10.1093/petrology/egi021
702 Langmuir, C.H., 1989. Geochemical consequences of in situ crystallization. Nature
703 340, 199–205. https://doi.org/10.1038/340199a0
704 Larsen, L.M., 1979. Distribution of REE and other trace elements between phenocrysts
705 and peralkaline undersaturated magmas, exemplified by rocks from the Gardar igneous
706 province, south Greenland. Lithos 12, 303–315. https://doi.org/10.1016/0024-4937(79)90022-
707 7
708 Le Maitre, R.W., Streckeisen, A., Zanettin, B., Le Bas, M.J., Bonin, B., Bateman, P.
709 (Eds.), 2002. Igneous Rocks: A Classification and Glossary of Terms: Recommendations of
710 the International Union of Geological Sciences Subcommission on the Systematics of Igneous
711 Rocks, 2nd ed. Cambridge University Press, Cambridge.
712 https://doi.org/10.1017/CBO9780511535581
713 Legendre, C., Maury, R.C., Caroff, M., Guillou, H., Cotten, J., Chauvel, C., Bollinger,
714 C., Hémond, C., Guille, G., Blais, S., Rossi, P., Savanier, D., 2005. Origin of Exceptionally
715 Abundant Phonolites on Ua Pou Island (Marquesas, French Polynesia): Partial Melting of

716 Basanites Followed by Crustal Contamination. Journal of Petrology 46, 1925–1962.
717 https://doi.org/10.1093/petrology/egi043
718 Lemarchand, F., Villemant, B., Calas, G., 1987. Trace element distribution coefficients
719 in alkaline series. Geochimica et Cosmochimica Acta 51, 1071–1081.
720 https://doi.org/10.1016/0016-7037(87)90201-8
721 LeMasurier, W.E., Futa, K., Hole, M., Kawachi, Y., 2003. Polybaric Evolution of
722 Phonolite, Trachyte, and Rhyolite Volcanoes in Eastern Marie Byrd Land, Antarctica: Controls
723 on Peralkalinity and Silica Saturation. International Geology Review 45, 1055–1099.
724 https://doi.org/10.2747/0020-6814.45.12.1055
725 Lesher, C.E., Spera, F.J., 2015. Chapter 5 - Thermodynamic and Transport Properties
726 of Silicate Melts and Magma, in: Sigurdsson, H. (Ed.), The Encyclopedia of Volcanoes
727 (Second Edition). Academic Press, Amsterdam, pp. 113–141. https://doi.org/10.1016/B978-0-
728 12-385938-9.00005-5
729 Li, X., Zhang, C., Behrens, H., Holtz, F., 2020. Calculating amphibole formula from
730 electron microprobe analysis data using a machine learning method based on principal
731 components regression. Lithos 362–363, 105469. https://doi.org/10.1016/j.lithos.2020.105469
732 Lucassen, F., Pudlo, D., Franz, G., Romer, R.L., Dulski, P., 2013. Cenozoic intra-plate
733 magmatism in the Darfur volcanic province: mantle source, phonolite-trachyte genesis and
734 relation to other volcanic provinces in NE Africa. International Journal of Earth Sciences 102,
735 183–205. https://doi.org/10.1007/s00531-012-0792-1
736 Marsh, B.D., 2002. On bimodal differentiation by solidification front instability in
737 basaltic magmas, part 1: basic mechanics. Geochimica et Cosmochimica Acta 66, 2211–2229.
738 https://doi.org/10.1016/S0016-7037(02)00905-5
739 Masotta, M., Mollo, S., 2019. A New Plagioclase-Liquid Hygrometer Specific to
740 Trachytic Systems. Minerals 9, 375. https://doi.org/10.3390/min9060375

741 Masotta, M., Freda, C., Gaeta, M., 2012. Origin of crystal-poor, differentiated magmas:
742 insights from thermal gradient experiments. Contrib Mineral Petrol 163, 49–65.
743 https://doi.org/10.1007/s00410-011-0658-8
744 Masotta, M., Mollo, S., Freda, C., Gaeta, M., Moore, G., 2013. Clinopyroxene–liquid
745 thermometers and barometers specific to alkaline differentiated magmas. Contrib Mineral
746 Petrol 166, 1545–1561. https://doi.org/10.1007/s00410-013-0927-9
747 Masotta, M., Mollo, S., Gaeta, M., Freda, C., 2016. Melt extraction in mush zones: The
748 case of crystal-rich enclaves at the Sabatini Volcanic District (central Italy). Lithos 248–251,
749 288–292. https://doi.org/10.1016/j.lithos.2016.01.030
750 McDonough, W.F., Sun, S. -s., 1995. The composition of the Earth. Chemical Geology,
751 Chemical Evolution of the Mantle 120, 223–253. https://doi.org/10.1016/0009-
752 2541(94)00140-4
753 McDougall, I., Coombs, D.S., 1973. Potassium-argon ages for the Dunedin volcano and
754 outlying volcanics. New Zealand Journal of Geology and Geophysics 16, 179–188.
755 https://doi.org/10.1080/00288306.1973.10431451
756 McLeod, O.E., White, J.D.L., 2018. Petrogenetic links between the Dunedin Volcano
757 and peripheral volcanics of the Karitane Suite. New Zealand Journal of Geology and
758 Geophysics 61, 543–561. https://doi.org/10.1080/00288306.2018.1518248
759 Meade, F.C., Troll, V.R., Ellam, R.M., Freda, C., Font, L., Donaldson, C.H.,
760 Klonowska, I., 2014. Bimodal magmatism produced by progressively inhibited crustal
761 assimilation. Nat Commun 5, 4199. https://doi.org/10.1038/ncomms5199
762 Molina, J.F., Montero, P., Bea, F., Scarrow, J.H., 2012. Anomalous xenocryst
763 dispersion during tonalite–granodiorite crystal mush hybridization in the mid crust:
764 Mineralogical and geochemical evidence from Variscan appinites (Avila Batholith, Central

765 Iberia). Lithos, Seventh Hutton Symposium on Granites and Related Rocks 153, 224–242.
766 https://doi.org/10.1016/j.lithos.2012.03.021
767 Mollo, S., Masotta, M., 2014. Optimizing pre-eruptive temperature estimates in
768 thermally and chemically zoned magma chambers. Chemical Geology 368, 97–103.
769 https://doi.org/10.1016/j.chemgeo.2014.01.007
770 Mollo, S., Putirka, K., Misiti, V., Soligo, M., Scarlato, P., 2013. A new test for
771 equilibrium based on clinopyroxene–melt pairs: Clues on the solidification temperatures of
772 Etnean alkaline melts at post-eruptive conditions. Chemical Geology 352, 92–100.
773 https://doi.org/10.1016/j.chemgeo.2013.05.026
774 Mollo, S., Masotta, M., Forni, F., Bachmann, O., De Astis, G., Moore, G., Scarlato, P.,
775 2015a. A K-feldspar–liquid hygrometer specific to alkaline differentiated magmas. Chemical
776 Geology 392, 1–8. https://doi.org/10.1016/j.chemgeo.2014.11.010
777 Mollo, S., Giacomoni, P.P., Coltorti, M., Ferlito, C., Iezzi, G., Scarlato, P., 2015b.
778 Reconstruction of magmatic variables governing recent Etnean eruptions: Constraints from
779 mineral chemistry and P–T–fO2–H2O modeling. Lithos 212–215, 311–320.
780 https://doi.org/10.1016/j.lithos.2014.11.020
781 Mollo, S., Giacomoni, P.P., Andronico, D., Scarlato, P., 2015c. Clinopyroxene and
782 titanomagnetite cation redistributions at Mt. Etna volcano (Sicily, Italy): Footprints of the final
783 solidification history of lava fountains and lava flows. Chemical Geology 406, 45–54.
784 https://doi.org/10.1016/j.chemgeo.2015.04.017
785 Namur, O., Charlier, B., Toplis, M.J., Vander Auwera, J., 2012. Prediction of
786 plagioclase-melt equilibria in anhydrous silicate melts at 1-atm. Contrib Mineral Petrol 163,
787 133–150. https://doi.org/10.1007/s00410-011-0662-z

Nekvasil, H., Dondolini, A., Horn, J., Filiberto, J., Long, H., Lindsley, D.H., 2004. The Origin and Evolution of Silica-saturated Alkalic Suites: an Experimental Study. J Petrology 45, 693–721. https://doi.org/10.1093/petrology/egg103

Palummo, F., Mollo, S., Astis, G.D., Stefano, F.D., Nazzari, M., Scarlato, P., 2020. Petrological and geochemical modeling of magmas erupted at Vulcano Island in the period 54–8 ka: Quantitative constraints on the sub-volcanic architecture of the plumbing system. Lithos 374–375, 105715. https://doi.org/10.1016/j.lithos.2020.105715

Panter, K.S., Kyle, P.R., Smellie, J.L., 1997. Petrogenesis of a Phonolite–Trachyte Succession at Mount Sidley, Marie Byrd Land, Antarctica. J Petrology 38, 1225–1253. https://doi.org/10.1093/petroj/38.9.1225

Panter, K.S., Wilch, T.I., Smellie, J.L., Kyle, P.R., McIntosh, W.C., 2021. Chapter 5.4b Marie Byrd Land and Ellsworth Land: petrology. Geological Society, London, Memoirs 55, 577–614. https://doi.org/10.1144/M55-2019-50

Park, J., Lim, H., Myeong, B., Jang, Y.-D., 2020. Syenite from Ulleung Island: As a window for pre-eruptive shallow alkaline magma dynamics. Lithos 356–357, 105342. https://doi.org/10.1016/j.lithos.2019.105342

Perinelli, C., Mollo, S., Gaeta, M., De, C.S.P., Palladino, D.M., Armienti, P., Scarlato, P., Putirka, K.D., 2016. An improved clinopyroxene-based hygrometer for Etnean magmas and implications for eruption triggering mechanisms. American Mineralogist 101, 2774–2777. https://doi.org/10.2138/am-2016-5916

Pontesilli, A., Brenna, M., Ubide, T., Mollo, S., Masotta, M., Caulfield, J., Le Roux, P., Nazzari, M., Scott, J.M., Scarlato, P., 2021. Intraplate basalt alkalinity modulated by a lithospheric mantle filter at the Dunedin Volcano (New Zealand). Journal of Petrology. https://doi.org/10.1093/petrology/egab062

Price, R.C., 1973. Geochemical investigations of the alkalic rocks of the Dunedin volcano, East Otago, New Zealand (Thesis). University of Otago.

Price, R.C., Compston, W., 1973. The geochemistry of the Dunedin Volcano: Strontium isotope chemistry. Contr. Mineral. and Petrol. 42, 55–61. https://doi.org/10.1007/BF00521647

Price, R.C., Chappell, B.W., 1975. Fractional crystallisation and the petrology of Dunedin volcano. Contr. Mineral. and Petrol. 53, 157–182. https://doi.org/10.1007/BF00372602

Price, R.C., Coombs, D.S., 1975. Phonolitic lava domes and other features of the Dunedin Volcano, East Otago. Journal of the Royal Society of New Zealand 5, 133–152. https://doi.org/10.1080/03036758.1975.10419368

Price, R.C., Cooper, A.F., Woodhead, J.D., Cartwright, I., 2003. Phonolitic Diatremes within the Dunedin Volcano, South Island, New Zealand. J Petrology 44, 2053–2080. https://doi.org/10.1093/petrology/egg070

Putirka, K.D., 2005. Igneous thermometers and barometers based on plagioclase + liquid equilibria: Tests of some existing models and new calibrations. American Mineralogist 90, 336–346. https://doi.org/10.2138/am.2005.1449

Putirka, K.D., 2008. Thermometers and Barometers for Volcanic Systems. Reviews in Mineralogy and Geochemistry 69, 61–120. https://doi.org/10.2138/rmg.2008.69.3

Putirka, K., Johnson, M., Kinzler, R., Longhi, J., Walker, D., 1996. Thermobarometry of mafic igneous rocks based on clinopyroxene-liquid equilibria, 0–30 kbar. Contrib Mineral Petrol 123, 92–108. https://doi.org/10.1007/s004100050145

Reilly, W.I., 1972. Gravitational expression of the Dunedin Volcano. New Zealand Journal of Geology and Geophysics 15, 16–21. https://doi.org/10.1080/00288306.1972.10423943

837 Reiners, P.W., Nelson, B.K., Ghiorso, M.S., 1995. Assimilation of felsic crust by
838 basaltic magma: Thermal limits and extents of crustal contamination of mantle-derived
839 magmas. Geology 23, 563–566. https://doi.org/10.1130/0091-
840 7613(1995)023<0563:AOFCBB>2.3.CO;2
841 Robie, R. A., Hemingway, B. S., & Fisher, J. R. (1995). Thermodynamic properties of
842 minerals and related substances at 298.15 K and 1 bar (105 Pascals) pressure and at higher
843 temperatures. US Geol. *Survey Bull*, *2131*, 461.Rollinson, H. R., 1994. Using geochemical
844 data: evaluation, presentation, interpretation. Routledge.
845 Scanlan, E.J., Scott, J.M., Roux, P.J. le, 2020. Pyrometamorphosed Otago Schist
846 xenoliths cause minor contamination of Dunedin Volcanic Group basanite. New Zealand
847 Journal of Geology and Geophysics 0, 1–17. https://doi.org/10.1080/00288306.2020.1767659
848 Schmidt, B.C., Behrens, H., 2008. Water solubility in phonolite melts: Influence of melt
849 composition and temperature. Chemical Geology, 8th Silicate Melt Workshop 256, 259–268.
850 https://doi.org/10.1016/j.chemgeo.2008.06.043
851 Scott, J.M., Pontesilli, A., Brenna, M., White, J.D.L., Giacalone, E., Palin, J.M., Roux,
852 P.J. le, 2020. The Dunedin Volcanic Group and a revised model for Zealandia's alkaline
853 intraplate volcanism. New Zealand Journal of Geology and Geophysics 0, 1–20.
854 https://doi.org/10.1080/00288306.2019.1707695
855 Sliwinski, J.T., Bachmann, O., Ellis, B.S., Dávila-Harris, P., Nelson, B.K., Dufek, J.,
856 2015. Eruption of Shallow Crystal Cumulates during Explosive Phonolitic Eruptions on
857 Tenerife, Canary Islands. Journal of Petrology 56, 2173–2194.
858 https://doi.org/10.1093/petrology/egv068
859 Spera, F.J., Bohrson, W.A., 2001. Energy-Constrained Open-System Magmatic
860 Processes I: General Model and Energy-Constrained Assimilation and Fractional

Crystallization (EC-AFC) Formulation. J Petrology 42, 999–1018. https://doi.org/10.1093/petrology/42.5.999

Stebbins, J.F., Carmichael, I.S.E., Moret, L.K., 1984. Heat capacities and entropies of silicate liquids and glasses. Contr. Mineral. and Petrol. 86, 131–148. https://doi.org/10.1007/BF00381840

Stormer, J.C., Nicholls, J., 1978. XLFRAC: a program for the interactive testing of magmatic differentiation models. Computers & Geosciences 4, 143–159. https://doi.org/10.1016/0098-3004(78)90083-3

Szymanowski, D., Wotzlaw, J.-F., Ellis, B.S., Bachmann, O., Guillong, M., von Quadt, A., 2017. Protracted near-solidus storage and pre-eruptive rejuvenation of large magma reservoirs. Nature Geoscience 10, 777–782. https://doi.org/10.1038/ngeo3020

Thiele, S.T., Cruden, A.R., Zhang, X., Micklethwaite, S., Matchan, E.L., 2021. Reactivation of Magma Pathways: Insights From Field Observations, Geochronology, Geomechanical Tests, and Numerical Models. Journal of Geophysical Research: Solid Earth 126, e2020JB021477. https://doi.org/10.1029/2020JB021477

Thompson, G., Smith, I., Malpas, J., 2001. Origin of oceanic phonolites by crystal fractionation and the problem of the Daly gap: an example from Rarotonga. Contrib Mineral Petrol 142, 336–346. https://doi.org/10.1007/s004100100294

Villemant, B., 1988. Trace element evolution in the Phlegrean Fields (Central Italy): fractional crystallization and selective enrichment. Contrib Mineral Petrol 98, 169–183. https://doi.org/10.1007/BF00402110

White, J.C., Espejel-García, V.V., Anthony, E.Y., Omenda, P., 2012. Open System evolution of peralkaline trachyte and phonolite from the Suswa volcano, Kenya rift. Lithos, Peralkaline Rocks and Carbonatites with Special Reference to the East African Rift 152, 84–104. https://doi.org/10.1016/j.lithos.2012.01.023

Wieser, P.E., Edmonds, M., Maclennan, J., Jenner, F.E., Kunz, B.E., 2019. Crystal scavenging from mush piles recorded by melt inclusions. Nature Communications 10, 5797. https://doi.org/10.1038/s41467-019-13518-2

Wolff, J.A., 2017. On the syenite-trachyte problem. Geology 45, 1067–1070. https://doi.org/10.1130/G39415.1

Wolff, J.A., Ellis, B.S., Ramos, F.C., Starkel, W.A., Boroughs, S., Olin, P.H., Bachmann, O., 2015. Remelting of cumulates as a process for producing chemical zoning in silicic tuffs: A comparison of cool, wet and hot, dry rhyolitic magma systems. Lithos 236–237, 275–286. https://doi.org/10.1016/j.lithos.2015.09.002

Wolff, J.A., Forni, F., Ellis, B.S., Szymanowski, D., 2020. Europium and barium enrichments in compositionally zoned felsic tuffs: A smoking gun for the origin of chemical and physical gradients by cumulate melting. Earth and Planetary Science Letters 540, 116251. https://doi.org/10.1016/j.epsl.2020.116251

Wright, J.B., 1971. The phonolite-trachyte spectrum. Lithos 4, 1–5. https://doi.org/10.1016/0024-4937(71)90110-1

Ziberna, L., Green, E.C.R., Blundy, J.D., 2017. Multiple-reaction geobarometry for olivine-bearing igneous rocks. American Mineralogist 102, 2349–2366. https://doi.org/10.2138/am-2017-6154

Figure captions

Figure 1. Synthesis map of the Dunedin Volcano with extent of volcanic units, sample locations and available geochronological data (Scott et al., 2020). List of sample coordinates is included in Supplementary Material S1. P = phonotephrite, T = tephriphonolite, M = mugearite, B = benmoreite.

911 **Figure 2.** Representative thin section photomicrographs in plane-polarized light (PPL) and
912 cross-polarized light (XPL). (a) Phenocryst assemblage of clinopyroxene + amphibole +
913 plagioclase in a groundmass of clinopyroxene + plagioclase + titanomagnetite from a highly
914 alkaline intermediate lava (phonotephrite PT2) (PPL). (b) Typical phonolite texture (sample
915 P4), with green clinopyroxene + alkali feldspar + resorbed amphibole in a groundmass of green
916 clinopyroxene + alkali feldspar + titanomagnetite. Euhedral green clinopyroxene overgrows a
917 pink resorbed core (PPL). (c) Phonolites may be highly porphyritic, including abundant alkali
918 feldspars and strongly resorbed amphibole crystals, whose resorption rims consist of green
919 clinopyroxene + titanomagnetite + alkali feldspar (PPL). (d) Syenite enclave FE3 (hosted by
920 tephriphonolite TP3), with phase assemblage mainly constituted by amphibole + alkali feldspar
921 (XPL). (e) Feldspar-rich cumulate FE1 (hosted by tephriphonolite TP1) containing large
922 quantities of alkali feldspar (≥1 mm) and brown-greenish amphibole, as well as minor green
923 clinopyroxene with resorbed pink core, (PPL). (f) Typical texture of trachytes, with few
924 phenocrysts of alkali feldspar + plagioclase (oligoclase) + amphibole. The groundmass is
925 dominated by alkali feldspars, showing flow alignment (PPL).
926
927 **Figure 3.** Backscattered electron (BSE) photomicrographs of representative phenocrysts
928 whose compositions are described in the text. (a) Di, Ts-rich clinopyroxene from phonotephrite
929 PT2. (b) Clinopyroxene in phonolite P3 showing a resorbed and internally zoned Di, Ts-rich
930 core overgrown by a Di, Ts-poor mantle. (c) Large amphibole phenocryst from phonotephrite
931 PT2 showing a relatively thin titanomagnetite + clinopyroxene + plagioclase reaction rim
932 (<100 μm). (d) Amphibole microphenocryst in phonolite P2, with a titanomagnetite + green
933 clinopyroxene + alkali feldspar reaction rims (slightly thicker than 100 μm), with grain sizes
934 decreasing toward phenocryst interior. (e) Amphibole in syenite FE3, showing homogeneous

interiors and very thin (up to few 10 μm) rim zoning toward Fe-rich compositions. (f) Alkali feldspar from trachyte T1 in contact with a small, rounded fragment of schist.

Figure 4. Compositional characterization of (a) clinopyroxene, (b) amphibole, (c) feldspars. An, Anorthite. Ab, Albite. Or, Orthoclase. Mg#, $Mg/(Mg+Fe^{2+})$ where all iron is expressed as Fe^{2+}. P = phonotephrite, T = tephriphonolite, M = mugearite, B = benmoreite.

Figure 5. (a) Chemical classification of whole-rock data according to the Total Alkali vs Silica (TAS) classification of Le Maitre et al. (2002), with compositional terms for sodic varieties of trachybasalt (hawaiite), basaltic trachyandesite (mugearite) and trachyandesite (benmoreite). (b-e) Selected major elements variation plots vs. SiO_2 for whole-rock data. Enclave data come from Allen (1974), Price et al. (2003), and Hoernle et al., (2006). Literature data on eruptive products from Scott et al. (2020) are shown for comparison. P = phonotephrite, T = tephriphonolite, M = mugearite, B = benmoreite.

Figure 6. Rare earth element (REE) plots normalized to chondrite CI according to McDonough & Sun (1995) for (a) highly alkaline rocks, and (b) mildly alkaline rocks. Incompatible trace elements normalized to primitive mantle according to McDonough & Sun (1995) of (c) highly alkaline rocks and (d) mildly alkaline rocks. P = phonotephrite, T = tephriphonolite, M = mugearite, B = benmoreite.

Figure 7. Crystallization pressures of magmas based on equilibrium crystal-melt pairs and expressed as probability density functions. Number of data in each sample group, as well as average and standard deviation values are included in Supplementary Material S5. Average

959 uncertainties are indicated by the error bars. P = phonotephrite, T = tephriphonolite, M =
960 mugearite, B = benmoreite.
961
962 **Figure 8.** Crystallization temperatures of magmas based on equilibrium crystal-melt pairs and
963 expressed as probability density functions. Number of data in each sample group, as well as
964 average and standard deviation values are included in Supplementary Material S5. Average
965 uncertainties are indicated by the error bars. P = phonotephrite, T = tephriphonolite, M =
966 mugearite, B = benmoreite.
967
968 **Figure 9.** Melt water contents and oxygen fugacity of magmas based on equilibrium crystal-
969 melt pairs and expressed as probability density functions. Number of data in each sample
970 group, as well as average and standard deviation values are included in Supplementary Material
971 S5. Average uncertainties are indicated by the error bars. P = phonotephrite, T =
972 tephriphonolite, M = mugearite, B = benmoreite.
973
974 **Figure 10.** Schematic representation of the temporal evolution of Dunedin Volcano plumbing
975 system, relatively to the differentiation of (a) mildly alkaline intermediate magmas to trachyte
976 and (b) highly alkaline magmas to phonolite. Insets refer to thin section photomicrographs
977 showing the main petrographic features described in text. At lower to middle crustal depths,
978 clinopyroxene + amphibole + plagioclase were segregated from intermediate magmas. As
979 magma rises towards the surface and differentiates, crystallization of a phase assemblage
980 including alkali feldspar at upper crustal levels leads to the evolution of trachytes and
981 phonolites. Trachytes were differentiated after assimilation of country rock lithologies and
982 segregation of significant volumes of alkali feldspars (a). Conversely, phonolites represent the
983 interstitial liquids of feldspar-rich mush zones in the upper crust, at the mature stage of

plumbing system evolution (b). P = phonotephrite, T = tephriphonolite, M = mugearite, B = benmoreite.

Figure 11. Rayleigh Fractional Crystallization (FC), in situ crystallization (ISC), and Assimilation and Fractional Crystallization (AFC) models. For details on model parameters see Supplementary Material S6. Whole-rock compositions, average crustal composition (Scanlan et al., 2020) and literature data from Scott et al. (2020) are reported. (a) Ba vs. Zr. (b) Sr vs. Rb. (c) Yb vs. La. (d) $\frac{Eu}{Eu^*}$ vs. Nb. In (e) and (f) ^{143}Nd / ^{144}Nd vs. ^{87}Sr / ^{86}Sr of intermediate lavas, phonolites, trachytes, and crystal-rich enclaves are age-corrected to 13 Ma. In (f) ^{87}Sr / ^{86}Sr vs. Rb/Sr, results from AFC modeling are compared with isotopic data from Price and Compston (1973) on phonolites and trachytes (Supplementary Material S3). P = phonotephrite, T = tephriphonolite, M = mugearite, B = benmoreite.

Figure 12. Energy Constrained - Assimilation and Fractional Crystallization (EC-AFC; Spera & Bohrson, 2001) and thermal modeling results on the formation of trachytic melts via intrusion of mildly alkaline magmas. (a) Mass fraction of assimilated country rock and solid residue of fractional crystallization as function of isotopic composition of the magma, according to the EC-AFC model. (b) Crustal assimilation occurs when the ratio of heat required to assimilate to heat released by magma is lower than 1. The thermal range is consistent with thermometric constraints, when largely crystallized mildly alkaline magmas evolves to trachyte, and provide enough heat to partially melt the country rock.

Table caption

Table 1: Phenocryst and groundmass mineralogy (minerals are reported in order of abundance), total phenocryst content, and initial Sr isotopic compositions of intermediate and

1009 evolved rock types at Dunedin Volcano. A complete list of all samples collected in this study
1010 is also included. For more details, see Supplementary Materials.

Figure1

Click here to access/download;Figure;figure1.jpg

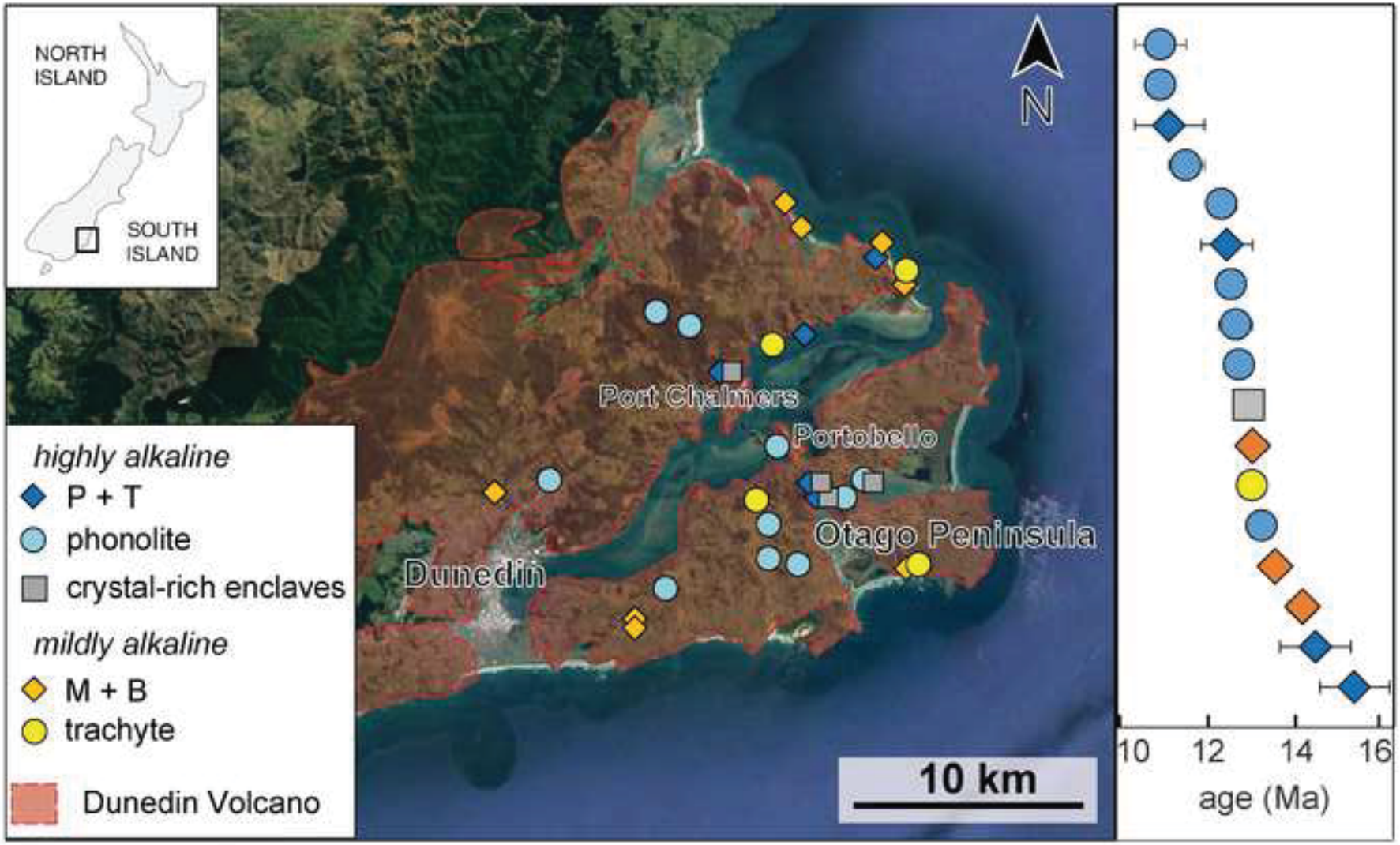

Figure2

Click here to access/download;Figure;figure2.jpg

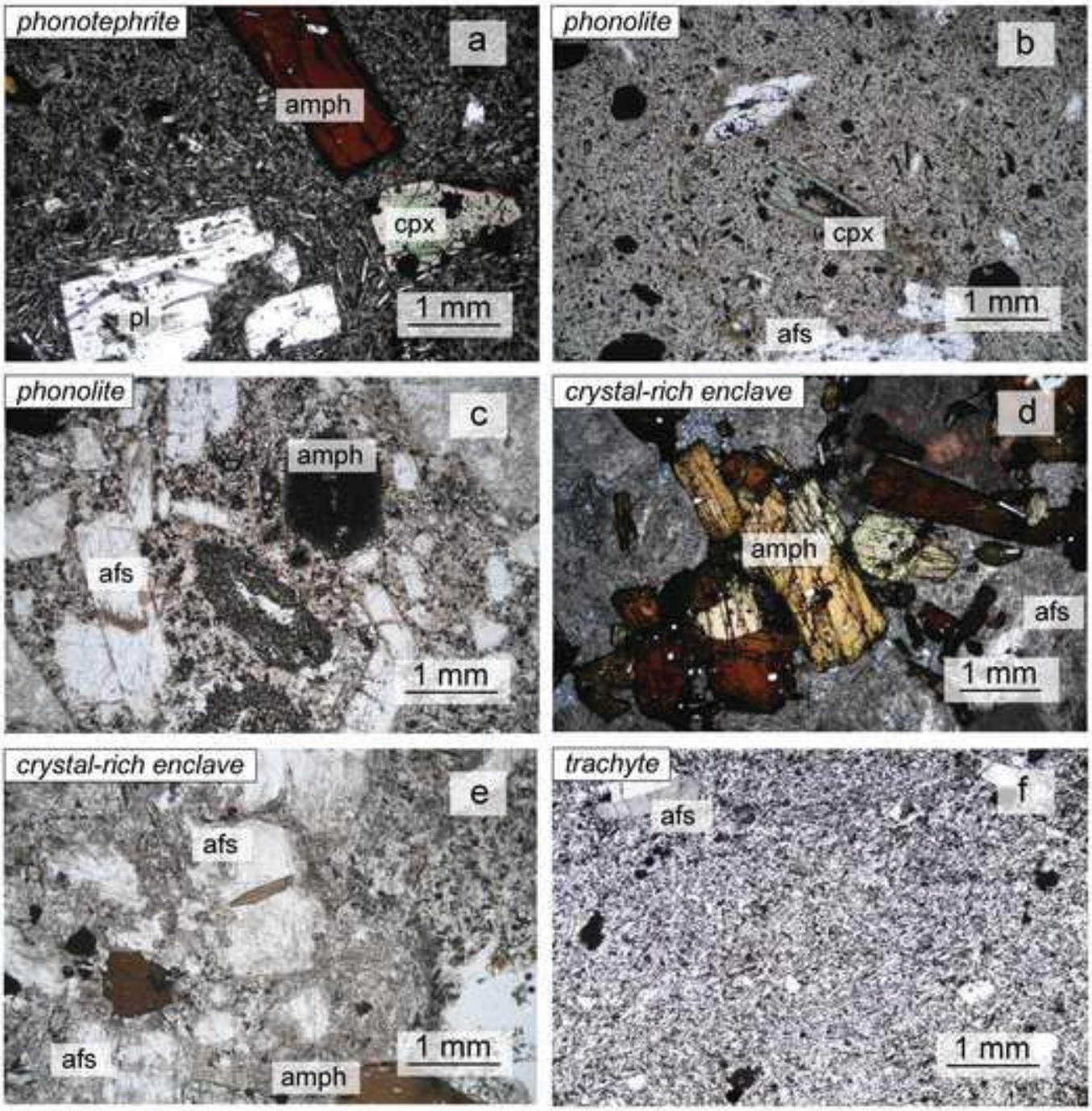

Figure3

Click here to access/download;Figure;figure3.jpg

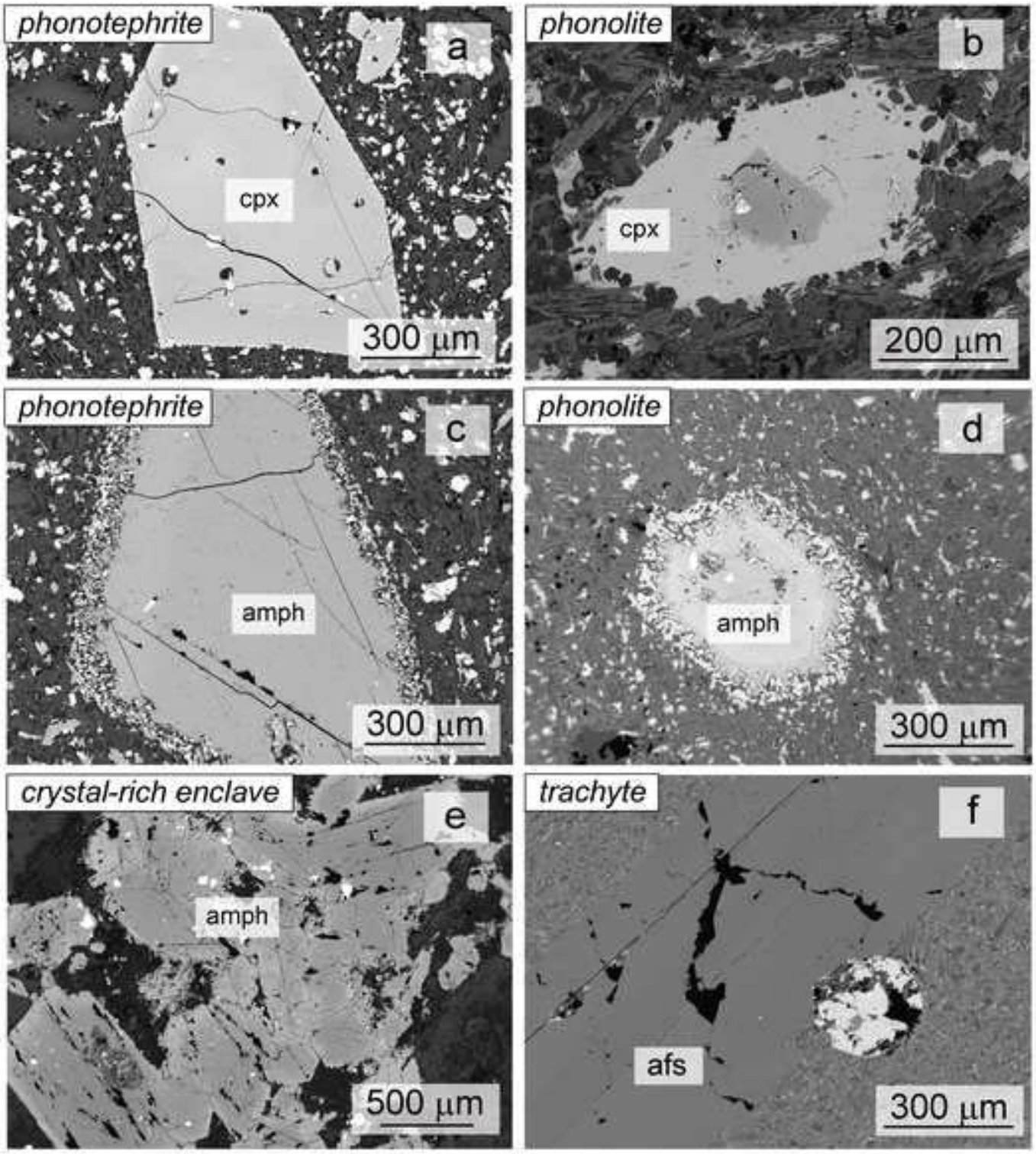

Figure4

Click here to access/download;Figure;figure4.jpg

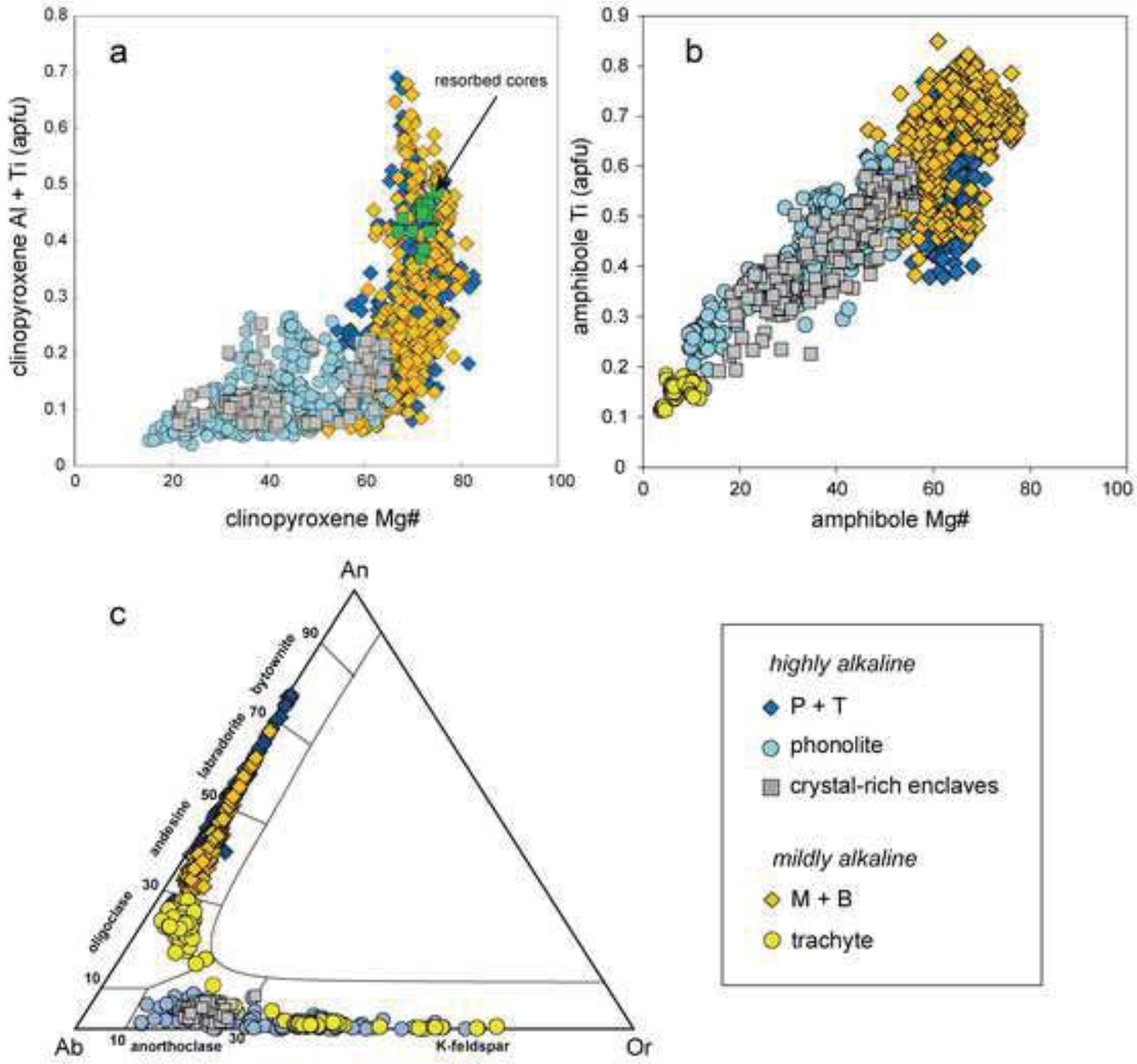

Figure5

Click here to access/download;Figure;figure5.jpg

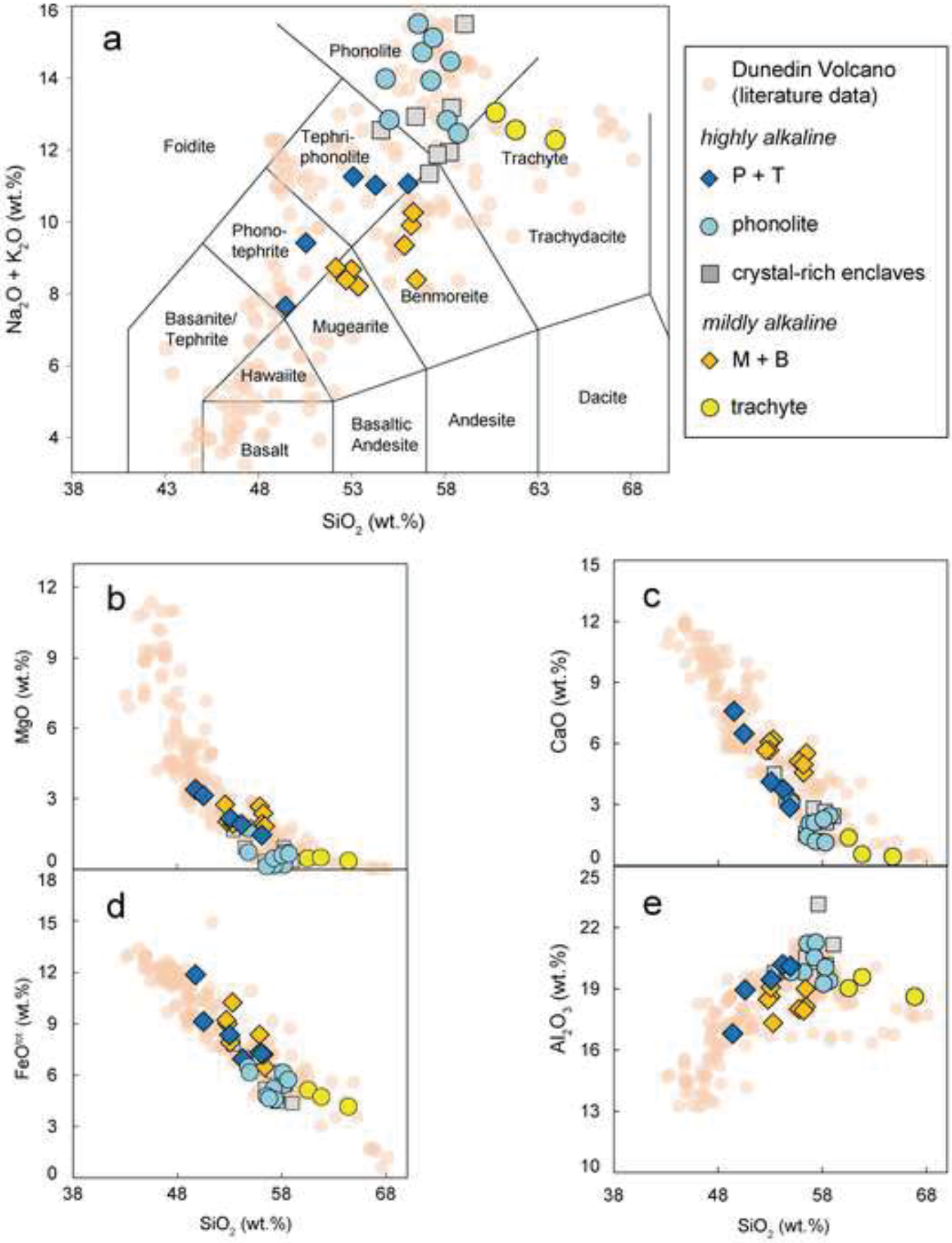

Figure6

Click here to access/download;Figure;figure6.jpg

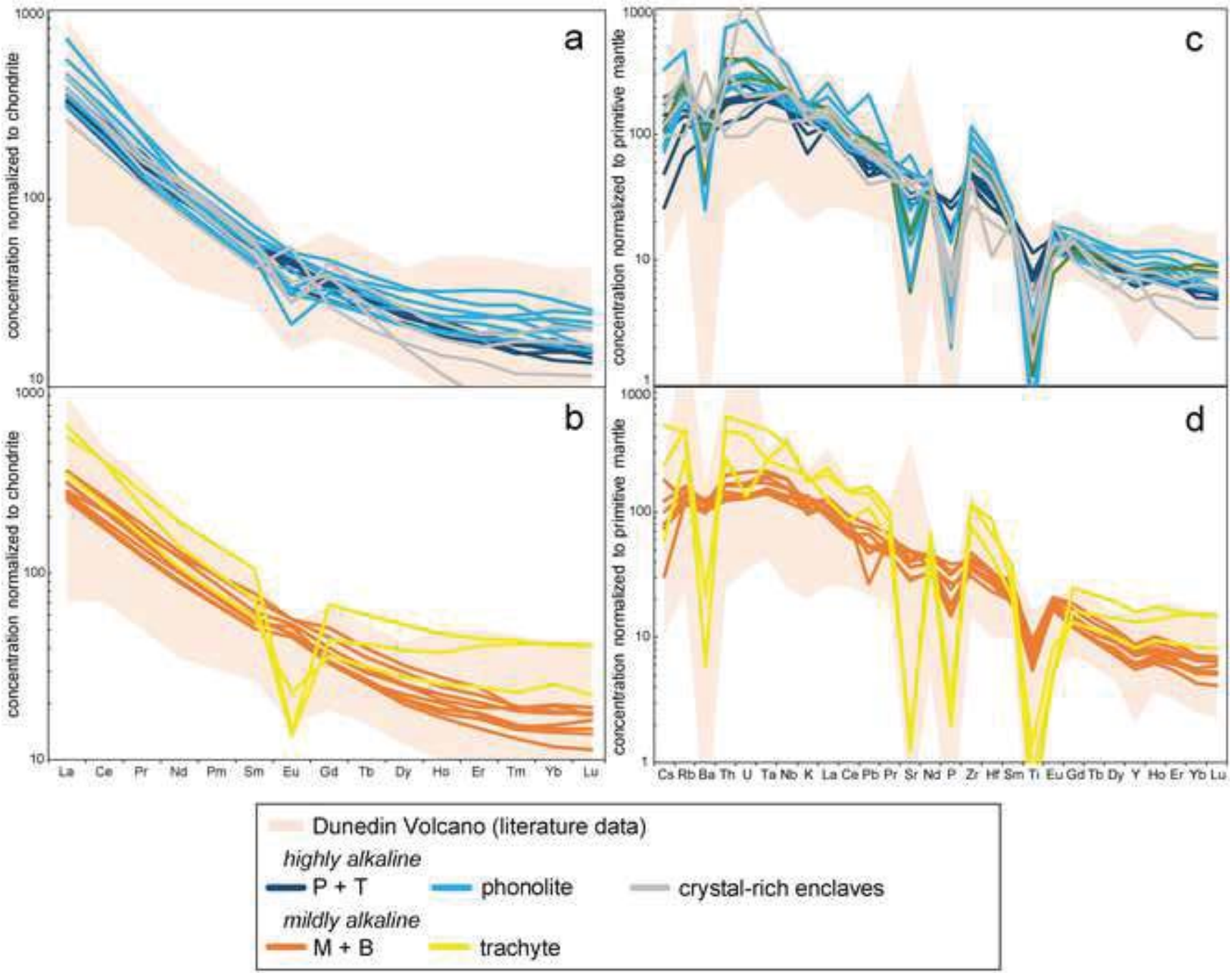

Figure7

Click here to access/download;Figure;figure7.jpg

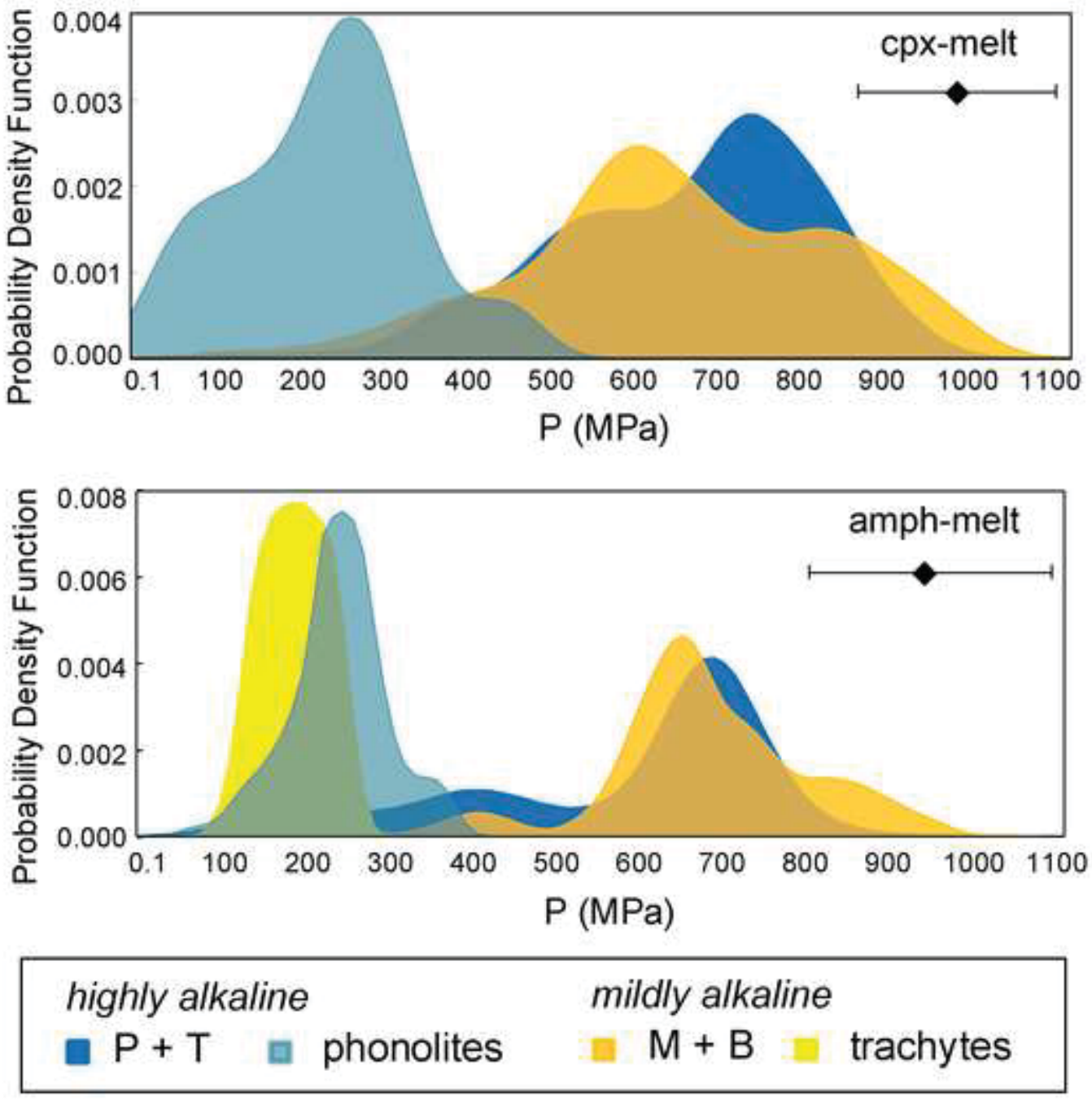

Figure8

Click here to access/download;Figure;figure8.jpg

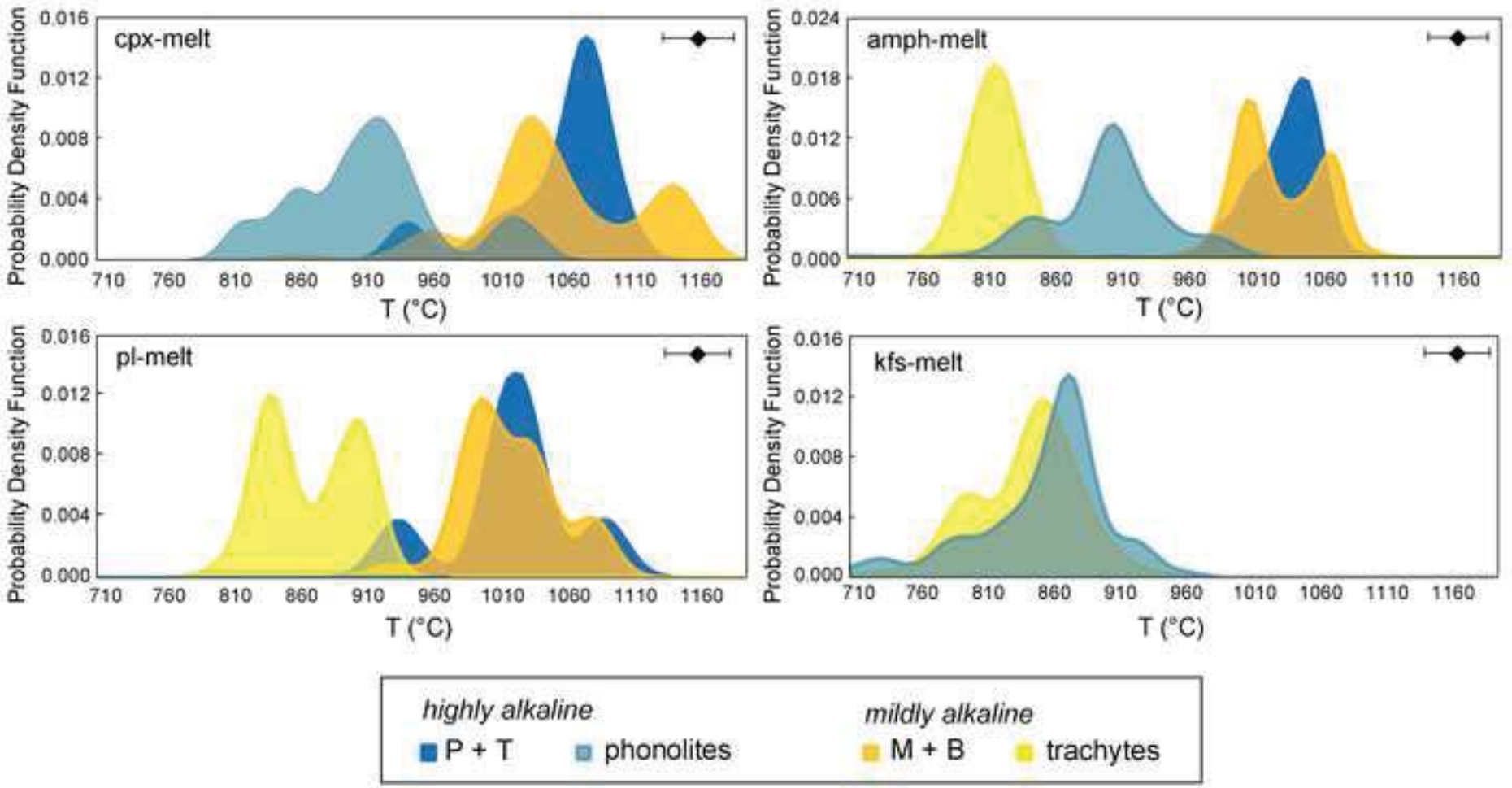

Figure9

Click here to access/download;Figure;figure9.jpg

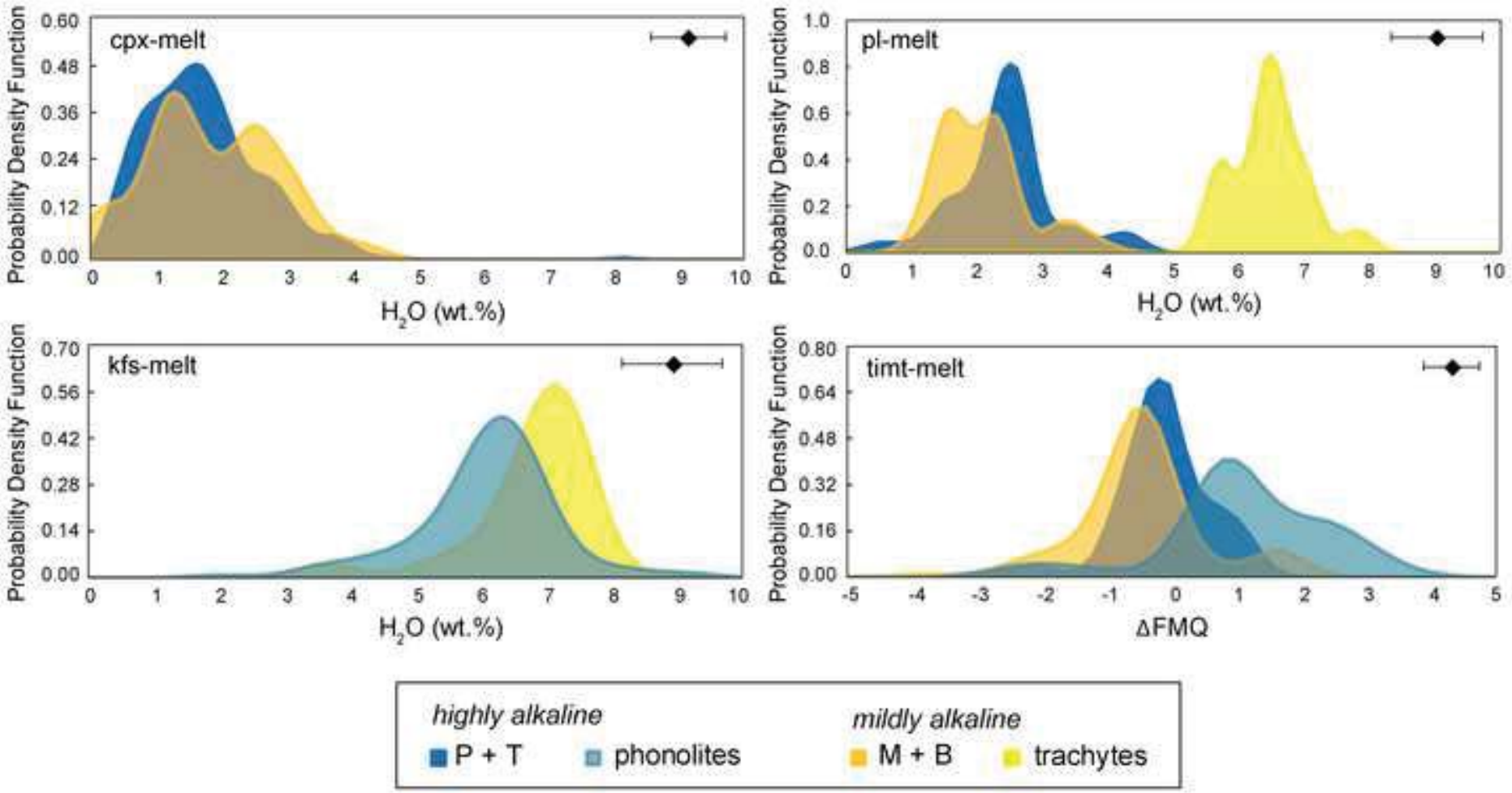

Figure10

Click here to access/download;Figure;figure10.jpg

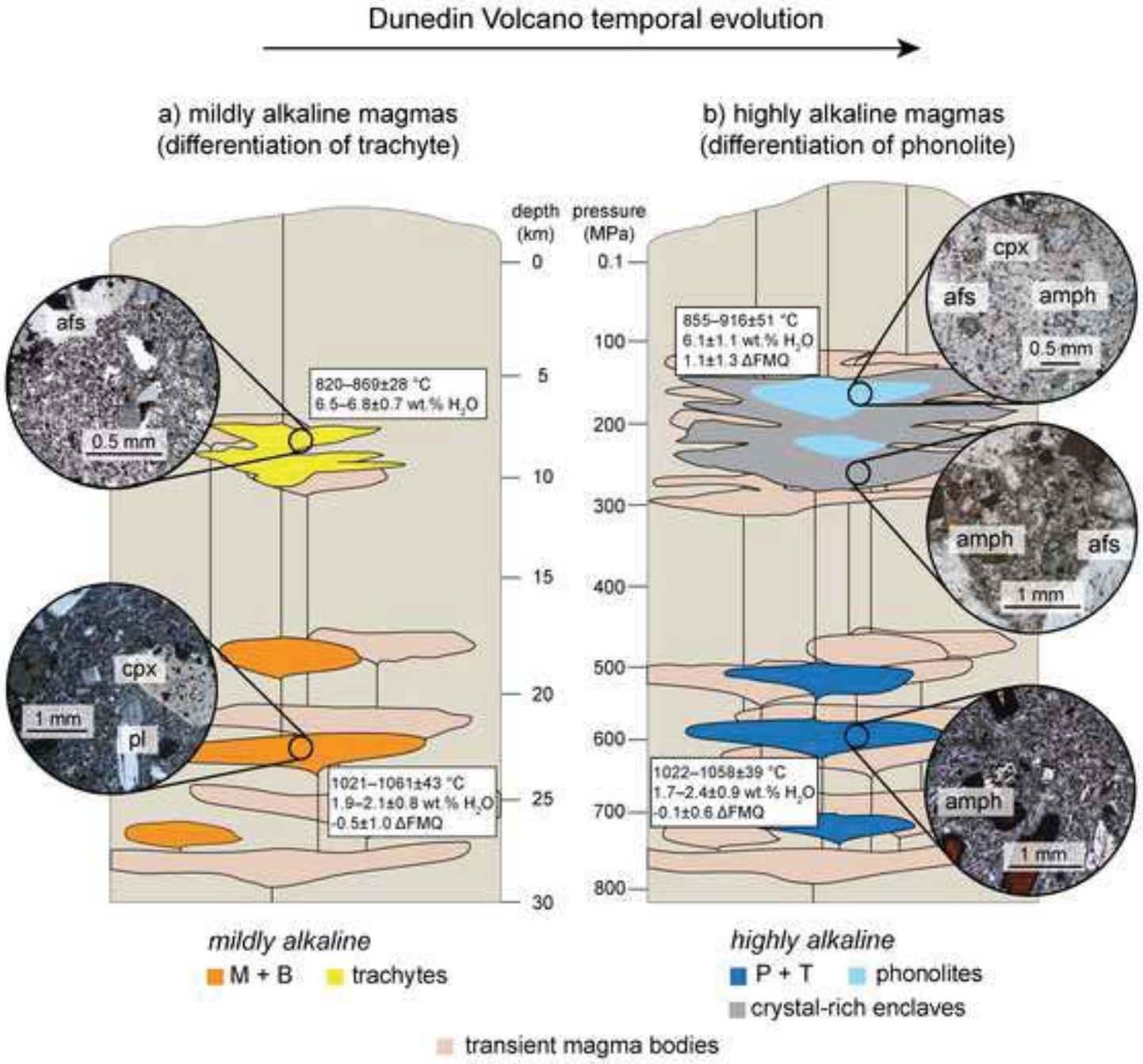

Figure11

Click here to access/download;Figure;figure11.jpg

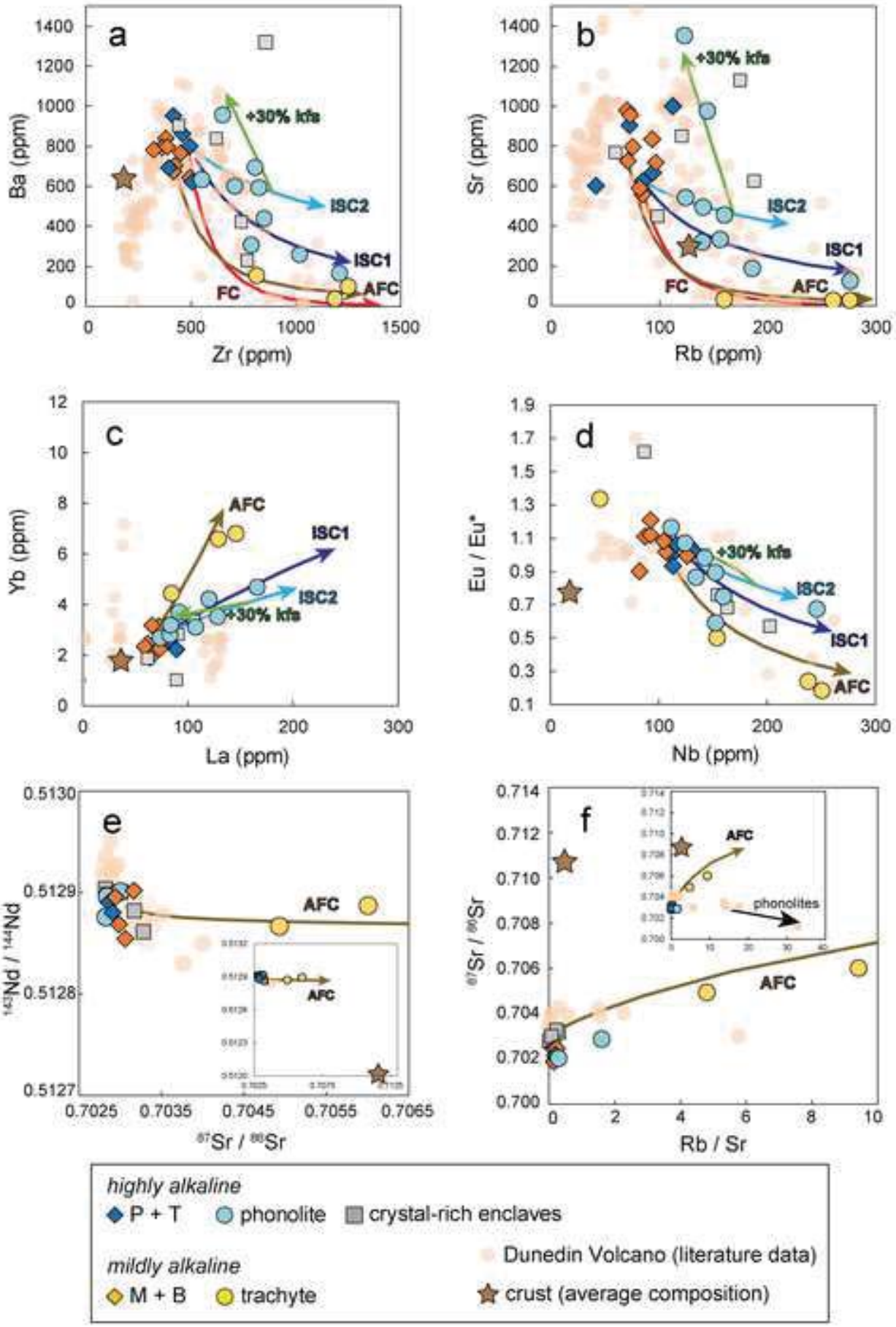

Figure12

Click here to access/download;Figure;figure12.jpg

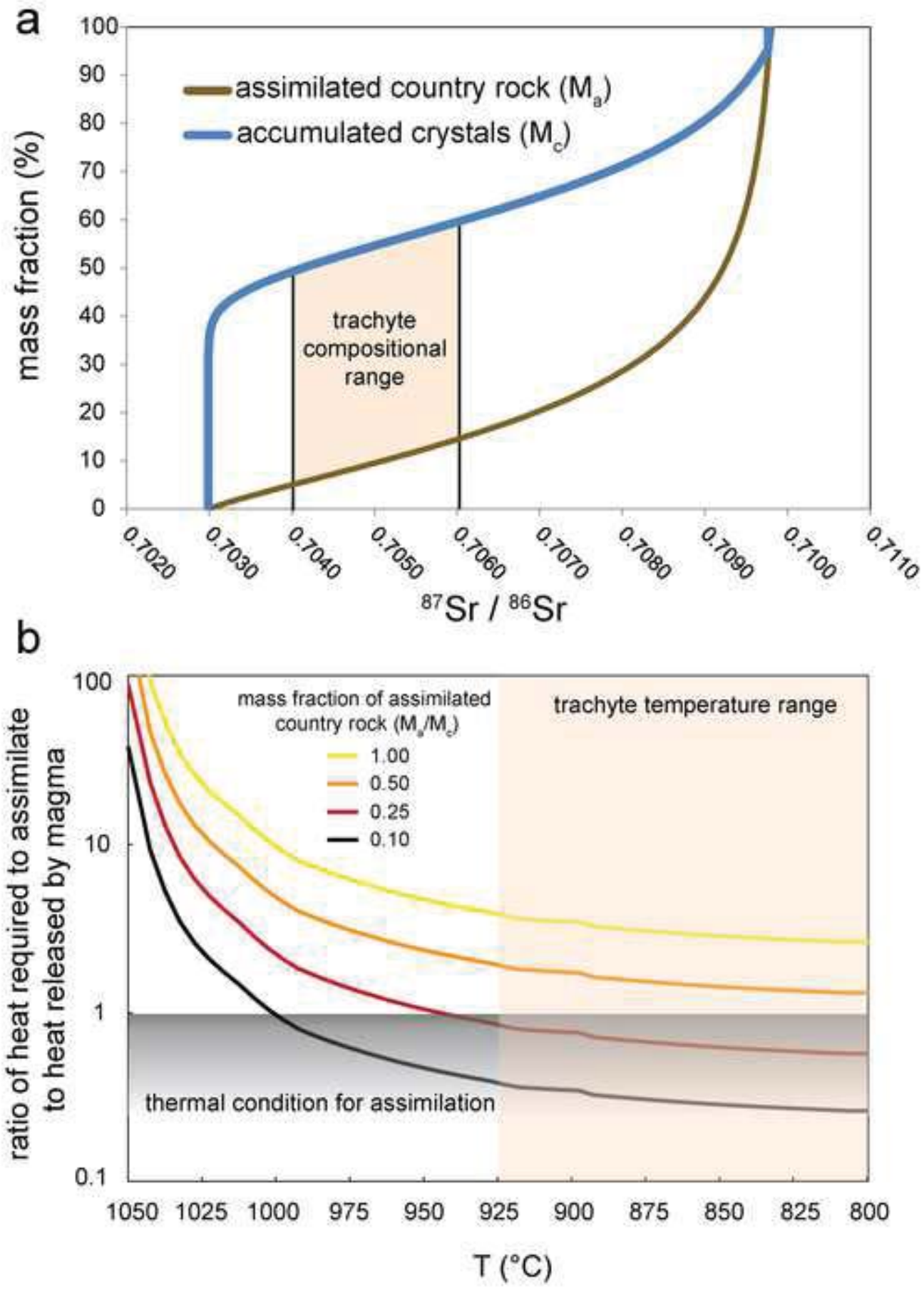

Table 1: Phenocryst and groundmass mineralogy (minerals are reported in order of abundance), total phenocryst content, and initial Sr isotopic compositions of intermediate and evolved rock types at Dunedin Volcano. A complete list of all samples collected in this study is also included. For more details, see Supplementary Materials.

rock series	rock type	phenocryst mineralogy	groundmass mineralogy	phenocryst content (vol.%)	$^{87}Sr/^{86}Sr_i$	list of samples
Highly alkaline series	intermediate rocks (phonotephrite, tephriphonolite)	Amphibole, clinopyroxene, plagioclase, titanomagnetite.	Plagioclase, clinopyroxene, titanomagnetite, apatite	16–28	0.7029	PT1, PT2, TP1, TP2, TP3
	phonolites	Alkali feldspar, clinopyroxene, amphibole, nepheline, titanomagnetite.	Alkali feldspar, clinopyroxene, titanomagnetite, apatite	7–43	0.7028–0.7029	P1, P2, P3, P4, P5, P6, P7, P8, P9
	crystal-rich enclaves	Alkali feldspar, clinopyroxene, amphibole, nepheline, titanomagnetite.	Alkali feldspar, clinopyroxene, titanomagnetite, apatite	62–100	0.7029–0.7033	FE1, FE2, FE3, FE4
Mildly alkaline series	intermediate rocks (mugearite, benmoreite)	Plagioclase, clinopyroxene, amphibole, titanomagnetite.	Plagioclase, clinopyroxene, titanomagnetite, apatite	11–31	0.7029–0.7032	M1, M2, M3, M4, B1, B2, B3, B4
	trachytes	Alkali feldspar, plagioclase, amphibole.	Alkali feldspar; minor titanomagnetite	6–10	0.7049–0.7060	T1, T2, T3